MDPI

*Article*

# Wake Effects on Wave-Induced Loads Acting on Cylinders in a Tripod Configuration

Michael Thome *, Ould el Moctar [ID] and Thomas E. Schellin [ID]

Institute of Ship Technology, Ocean Engineering and Transport Systems, Department of Mechanical and Process Engineering, University of Duisburg-Essen, 47057 Duisburg, Germany
* Correspondence: michael.thome@uni-due.de

**Abstract:** Comparative hydrodynamic loads caused by a focused wave acting on differently sized slender vertical cylinders placed in a wave canal were predicted at model scale using an unsteady Reynolds-averaged Navier–Stokes (URANS) solver and the Morison equation. This paper focused, first, on wake effects that need to be considered for the structural design of tripod configurations and, second, on the influence of these wake effects on wave-induced loads. For the Morison approach, flow velocities were gathered at incremental representative locations along the length of the cylinders, whereby the use of a central differencing approach obtained the associated flow accelerations. A first scenario dealt with a small- and a large-diameter cylinder, implemented individually at two immersion depths. A second scenario considered medium- and large-diameter cylinders arranged in a tripod configuration, where the upstream and downstream cylinders had the same diameter. For the single cylinder, impact loads obtained by both methods compared favorably to experimental measurements. For the tripod configuration, however, impact loads obtained by both methods differed due to the influence of wake effects. Thus, it was necessary to determine the influence of wake effects to assess the structural integrity of tripod configurations.

**Keywords:** hydrodynamics; CFD; numerical simulations; volume of fluid; URANS simulations; Morison equation; Keulegan–Carpenter number; two-phase flow; wake field

## 1. Introduction

Slender cylindrical structures are widely used not only for offshore structures and wind tower foundations, but also for so-called pump towers in liquefied natural gas (LNG) tanks. Such towers are subject to sloshing-induced hydrodynamic impact loads. To reliably assess these loads, computational fluid dynamics (CFD) simulations or experimental investigations are generally performed. Besides these relatively elaborate computations, using the well-known Morison equation [1] offers an efficient method to approximate hydrodynamic loads acting on cylindrical structures:

$$dF = \rho C_M \frac{dU}{dt} A \cdot dS + \frac{1}{2} \rho C_D U |U| D \cdot dS, \tag{1}$$

where $dF$ represents the force per segment length, $\rho$ is the density of the fluid phase, $C_M$ is the inertia coefficient, $U$ is the flow velocity, $t$ is time, $\frac{dU}{dt}$ is the acceleration of the flow, $A$ is the cross-sectional area of the cylinder, $dS$ is the cylinder's segment length, $C_D$ is the drag coefficient, and $D$ is the cylinders diameter.

When using the Morison equation, the structure itself is not directly part of the numerical flow model, i.e., the presence of the structure does not affect the water particle kinematics. The geometry, flow velocity, flow acceleration, fluid density, and drag and inertia coefficients must be specified at the location of the missing structure and inserted into the Morison equation. Keulegan and Carpenter were amongst the first to perform

experiments to determine drag and inertia coefficients [2]. They introduced the dimensionless Keulegan and Carpenter parameter $K_C$ to relate the amplitude of the oscillating wave velocity, the wave period, and the cylinder's diameter. Sarpkaya later introduced a new parameter $\beta$ relating $K_C$ and the Reynolds number $Re$ [3].

As sloshing tests in a model tank provide mainly statistical data on sloshing-induced impact loads acting on pump towers [4–7], it is difficult to precisely understand all physical phenomena necessary to accurately predict these loads. Impact loads occur quickly and are susceptible to local flow conditions [8]. Therefore, we decided to model the effect of a predefined focused wave acting on a pump tower configuration at a specific location in a wave canal. This enabled us to better observe and pinpoint local phenomena.

The hydrodynamic loads acting on a tripod configuration consisting of three cylinders were considered, where two downstream cylinders were located in the wake of an upstream cylinder. The upstream cylinder generated a wake field and, depending on the flow's Reynolds number and the distance between the upstream and downstream cylinders, this wake may influence the loads acting on the downstream cylinders. In the wake field, the fluid's mean velocities were less than the free stream velocities [9], thereby reducing the drag forces acting on the downstream cylinders [10,11].

An increase of wave loads was observed for cylinders installed side by side [12]. These loads were higher for regular non-breaking waves than for irregular non-breaking waves that were generated from a JONSWAP spectrum. Experimental investigations yielded modified drag and inertia coefficients for cylinders that were installed either in tandem or side by side [13]. Without calculating loads, numerical simulations with two side-by-side circular cylinders of Li et al. [14] illustrated the influence of the gap between the cylinders for a free surface flow. Tong et al. [15] investigated a steady uniform flow around two staggered cylinders at a low Reynolds number of $Re = 1 \times 10^3$. The presence of a second cylinder altered the pressure distribution and the location of stagnation points on the surface of both cylinders. A reciprocal influence between an upstream and a downstream cylinder was also observed when the spacing ratio $\frac{L}{D}$ (with $L$ being the distance of the center between the cylinders) was less than 3.5 for $Re = 5.8 \times 10^4$, equal to 3.5 for $Re = 8.3 \times 10^4$, and slightly higher than 3.5 for $Re = 1.1 \times 10^5$ [16] for cylinders being installed in tandem. Zdravkovich investigated the influence on the drag coefficient for different spacing ratios between two cylinders that were installed in tandem. He found that the influence of the downstream cylinder on the upstream cylinder is significant when the spacing ratio is less than 3.5 for subcritical Reynolds numbers [17].

This paper dealt with the investigation of hydrodynamic loads on single cylinders and cylinders arranged in a tripod configuration. The Morison equation was used to calculate the wave loads on the cylinders in undisturbed waves. These wave loads were compared to those acting on the cylinders in disturbed waves, where all cylinders were geometrically modeled. For the configuration consisting of large-sized cylinders, Reynolds numbers ranged between $Re = 5.0 \times 10^4$ and $Re = 1.6 \times 10^5$; for the configuration consisting of medium-sized cylinders, the Reynolds numbers ranged between $Re = 4.3 \times 10^4$ and $Re = 1.3 \times 10^5$. The tripod configuration represented a simplified LNG pump tower structure with staggered and side by side arrangements of the cylinders.

Using a turbulence model, the validation study was performed for the case with a single cylinder and presented in our conference paper [11]. It was summarized in this paper and extended by an additional validation study, also using a laminar flow model.

## 2. Test Case Description

The experiments of hydrodynamic loads acting on the cylinders were performed in a wave canal of 0.65 m width and 16.77 m length [18]. The initial water level was 0.667 m. A hydraulically powered flat-type wave maker generated the focused waves. A vertical wall installed at a distance of 12.53 m from the wave maker limited the tank's test length.

The first scenario comprised tests of two single steel cylinders situated vertically in the canal at a longitudinal distance of 11.62 m from the wave maker and 0.91 m from the rear

wall. A six degrees-of-freedom load sensor was fixed to a flange mounted at the top of each cylinder. This load sensor was enclosed in a frame whose height position was adjustable. Both cylinders had a length of 0.80 m, but they were each fixed at two different height positions to enable investigating impact loads at different immersion depths. In their low positions, the lower end of the cylinders was situated 0.198 m above the tank's bottom; in their high positions, 0.398 m above the tank's bottom. The small cylinder's diameter was $D_{small} = 0.0889$ m; the large cylinder's diameter was $D_{large} = 0.1524$ m. The purpose of these first scenario tests was to compare experimental data with numerical predictions.

The second scenario dealt with hydrodynamic loads acting on the cylinders in a tripod configuration, immersed to a depth of 0.469 m below the free surface. In this scenario, the investigated diameters were $D_{medium} = 0.1230$ m and $D_{large} = 0.1524$ m. The longitudinal distance between the center of the downstream cylinders and the rear wall was 0.91 m. The longitudinal distance between the center of the downstream cylinders and the upstream cylinder was two times the diameter. The upstream cylinder was located on the centerline of the wave canal and the downstream cylinder was located one diameter transversally from this centerline. The upstream and downstream cylinders always had the same diameter.

## 3. Experimental Setup

An MC12 series AMTI multi-component transducer was used to measure hydrodynamic loads at a sampling frequency of 2000 Hz [18]. This transducer's load capacity ranged between 100 N and 250 N for forces in the vertical direction, between 50 N and 125 N for forces in the longitudinal and transverse directions, between 50 Nm and 125 Nm for torques about the vertical axis, and between 100 Nm and 250 Nm for torques about the longitudinal and transverse directions. The load sensor was rigidly bolted on a movable support mounted above the wave canal. With this movable support, the sensor could be adjusted along the vertical axis to keep the single cylinder at the low and the high position. The cylinders were bolted through a fixation plate to the longitudinal center of the sensor [18].

To account for the effect of Newtonian viscosity, the non-breaking focused wave was generated on the basis of the Ricker spectrum with a peak period of $T_P = 2.617$ s. The focal point of the focused wave was set at a longitudinal distance of $x = 11.69$ m from the wave maker [18]. The position of the focal point was thus close to the center of the cylinders in the first scenario; specifically, it was positioned at a distance of 11.62 m from the wave maker. Table 1 lists the focused wave's greatest height of $A_w = 0.214$ m and the two parameters of $m = 1.42$ and $T = 0.2285$, which had to be specified to generate this wave in the first and second scenarios.

**Table 1.** Parameters of the wave for the first and second scenarios.

| $A_w$ (m) | $m$ | $x$ (m) | $T$ | $T_P$ (s) |
|---|---|---|---|---|
| 0.214 | 1.42 | 11.69 | 0.2285 | 2.617 |

## 4. Numerical Method

An Eulerian approach defined our liquid–gaseous two-phase flow according to the volume of fluid (VoF) method:

$$\alpha_i = \frac{V_i}{V},\qquad(2)$$

where $\alpha_i$ is the volume fraction of phase $i$, $V_i$ is the volume of the respective phase $i$, and $V$ is the volume of the cell.

Velocities, pressures, etc., were calculated for each grid cell of the computational domain. An appropriate coordinate system was defined to identify the location and time assigned to each liquid and gaseous particle of the respective cell [19]. Energy, mass, and momentum had to be conserved. For the prevailing two-phase flow, exchange terms for

energy, momentum, and mass accounted for the interactions of the two phases [20]. The term for the continuity equation is defined as follows:

$$\frac{\partial}{\partial t}\left(\int_V \rho dV\right) + \oint_A \rho v \cdot da = \int_V \sum_i S_{\alpha_i} \cdot \rho_i dV, \tag{3}$$

where $v$ is the mass-averaged velocity, and $a$ is the surface area. The product $S_{\alpha_i} \cdot \rho_i$ accounts for the phase source term in the mass source term. The term for the momentum equation is defined as follows:

$$\frac{\partial}{\partial t}\left(\int_V \rho v dV\right) + \oint_A \rho v \otimes v \cdot da = -\oint_A p\mathbf{I} \cdot da + \oint_A \mathbf{T} \cdot da + \int_V \rho g dV + \int_V f_b dV - \sum_i \alpha_i \rho_i v_{d,i} \otimes v_{d,i} \cdot da, \tag{4}$$

where $p$ is the pressure, $\mathbf{I}$ is the unity tensor, $\mathbf{T}$ is the viscous stress tensor, $g$ is the gravity, $f_b$ is the vector of the body forces, and $v_{d,i}$ is the diffusion velocity. The term for the energy equation is defined as follows:

$$\frac{\partial}{\partial t}\left(\int_V \rho E dV\right) + \oint_A \left[\rho v H + p + \sum_i \alpha_i \rho_i H_i v_{d,i}\right] \cdot da = -\oint_A \dot{q}'' \cdot da + \oint_A \mathbf{T}v \cdot da + \int_V f_b v dV + \int_V S_E dV, \tag{5}$$

where $E$ is the total energy, $H$ is the total enthalpy, $\dot{q}''$ is the heat flux vector, and $S_E$ is a user-defined energy source term.

The simulations for the first scenario were performed with a turbulence model as well as with a laminar model to investigate the necessity of using a turbulence model for the single cylinder case. The simulations for the second scenario were performed solely with the turbulence model because the wake generated by the upstream cylinder affected the downstream cylinders of the tripod configuration.

As it was necessary to employ an unsteady approach to simulate the two-phase flow, the VoF method was combined with a URANS solver for the turbulence model and only with the Navier–Stokes (NS) equations for the laminar model. An averaged value of the velocity, the pressure, the viscous stress tensor, the total energy, and the heat flux was implemented in the URANS calculations. This resulted in a change of the terms for the conservation equations. The continuity equation was written as follows:

$$\frac{\partial}{\partial t}\left(\int_V \rho dV\right) + \oint_A \rho \overline{v} \cdot da = \int_V \sum_i S_{\alpha_i} \cdot \rho_i dV, \tag{6}$$

where $\overline{v}$ is the averaged velocity. The momentum equation was changed to:

$$\frac{\partial}{\partial t}\left(\int_V \rho \overline{v} dV\right) + \oint_A \rho \overline{v} \otimes \overline{v} \cdot da = -\oint_A \overline{p}\mathbf{I} \cdot da + \oint_A (\overline{\mathbf{T}} + \mathbf{T}_{RANS}) \cdot da + \int_V \rho g dV + \int_V f_b dV - \sum_i \alpha_i \rho_i \overline{v}_{d,i} \otimes \overline{v}_{d,i} \cdot da, \tag{7}$$

where $\overline{p}$ is the averaged pressure, $\overline{\mathbf{T}}$ is the averaged viscous stress tensor, and $\overline{v}_{d,i}$ is the averaged diffusion velocity. A RANS stress tensor $\mathbf{T}_{RANS}$ was added to the mean viscous stress tensor in the momentum equation:

$$\mathbf{T}_{RANS} = -\rho \begin{pmatrix} \overline{u'u'} & \overline{u'v'} & \overline{u'w'} \\ \overline{v'u'} & \overline{v'v'} & \overline{v'w'} \\ \overline{w'u'} & \overline{w'v'} & \overline{w'w'} \end{pmatrix} + \frac{2}{3}\rho k\mathbf{I}, \tag{8}$$

where $u'$, $v'$, and $w'$ are the fluctuating components of the velocity along the $x$-, $y$-, and $z$-axis, and $k$ is the turbulent kinetic energy. The RANS stress tensor was also implemented in the energy conservation equation:

$$\frac{\partial}{\partial t}\left(\int_V \rho \overline{E} dV\right) + \oint_A \left[\rho \overline{v} H + \overline{p} + \sum_i \alpha_i \rho_i H_i \overline{v}_{d,i}\right] \cdot da = -\oint_A \overline{\dot{q}}'' \cdot da + \oint_A (\overline{\mathbf{T}} + \mathbf{T}_{RANS})\overline{v} \cdot da + \int_V f_b \overline{v} dV + \int_V S_E dV, \tag{9}$$

where $\overline{E}$ is the averaged total energy and $\overline{\dot{q}}''$ is the averaged heat flux vector.

The conservation equations of momentum and mass were solved consecutively with the segregated flow solver. The segregated flow solver relied on a semi-implicit method for

pressure linked equations (SIMPLE) algorithm to couple the pressure and velocity fields. With the predictor-corrector approach, a pressure correction equation generated a velocity field that satisfied the continuity equation. This pressure correction equation consisted of parts of the momentum and continuity equations. A pressure gradient $p_f$ was computed and replaced the pressure in the momentum equations:

$$p_f = \frac{\overline{a_0} p_{f0} + \overline{a_1} p_{f1}}{\overline{a_0} + \overline{a_1}}, \tag{10}$$

where $\overline{a_0}$ and $\overline{a_1}$ denote the average for each of the coefficients in the momentum equation for two adjacent cells 0 and 1, and $p_{f0}$ and $p_{f1}$ are face values that were interpolated from reconstructed gradients and cell values. The continuity equation was rewritten for the pressure–velocity coupling:

$$\sum_f \left( \dot{m_f}^* + \dot{m_f}' \right) = 0, \tag{11}$$

where $\dot{m_f}^*$ is the uncorrected face mass flux, which was obtained by solving the discrete momentum equations with an approximated pressure field $p^*$. As the continuity was not yet satisfied with the approximated pressure field, it needed the corrected mass term $\dot{m_f}'$:

$$\dot{m_f}' = Q_f \left( \dot{p_0}' - \dot{p_1}' \right) + \frac{\dot{m_f}^*}{\rho_f} \left( \frac{\partial \rho}{\partial p} \right)_T p'_{upwind}, \tag{12}$$

where $\dot{p_0}'$ and $\dot{p_1}'$ are the cell pressure corrections. The uncorrected mass flux $\dot{m_f}^*$ is then defined as follows:

$$\dot{m_f}^* = \rho_f a \left( \frac{v_0^* + v_1^*}{2} \right) - \gamma_f, \tag{13}$$

where $v_0^*$ and $v_1^*$ are the velocities after solving the discrete momentum equations with the approximated pressure field. The Rhie–Chow dissipation factor $\gamma_f$ prevents the development of physically unrealistic checker boarding of pressure caused by the linear interpolation from the cell centers to the faces of the cells:

$$\gamma_f = Q_f \left( p_1 - p_0 - \overline{\nabla p_f^*} \cdot ds \right), \tag{14}$$

where $\overline{\nabla p_f^*}$ is the volume-weighted average of the cell gradients of pressure and $Q_f$ defined as follows:

$$Q_f = \rho_f \left( \frac{V_0 + V_1}{\overline{a_0} + \overline{a_1}} \right) \boldsymbol{\alpha} \cdot \boldsymbol{a}, \tag{15}$$

where $p'_{upwind}$ is defined as:

$$p'_{upwind} = \begin{cases} p_0' & for \ \dot{m_f}^* > 0 \\ p_1' & for \ \dot{m_f}^* < 0 \end{cases}, \tag{16}$$

In the URANS simulations, the shear stress transport (SST) $k$–$\omega$ model of Menter [21] was used to solve for turbulence. The term for the transport equations for the kinetic energy $k$ was:

$$\frac{\partial}{\partial t}(\rho k) + \nabla(\rho k \overline{v}) = \nabla[(\mu + \sigma_k \mu_t)\nabla k] + P_k - \rho \beta^* f_{\beta^*}(\omega k - \omega_0 k_0) + S_k, \tag{17}$$

where $\mu$ is the dynamic viscosity, $\sigma_k$ is a model coefficient, $\mu_t$ is the turbulent eddy viscosity, $P_k$ is a sum of production terms consisting of a turbulent, a buoyancy and a non-linear production term, $\beta^*$ is a model coefficient, $f_{\beta^*}$ is a free-shear modification factor, $\omega$ is the specific dissipation rate, $\omega_0$ and $k_0$ are ambient turbulence values to counteract the

turbulence decay, and $S_k$ are the user-specified source terms. The term for the transport equations for the specific dissipation rate $\omega$ was:

$$\frac{\partial}{\partial t}(\rho\omega) + \nabla(\rho\omega\overline{\boldsymbol{v}}) = \nabla[(\mu + \sigma_\omega\mu_t)\nabla\omega] + P_\omega - \rho\beta f_\beta\left(\omega^2 - \omega_0^2\right) + S_\omega, \tag{18}$$

where $P_\omega$ is a sum of production terms consisting of a specific dissipation production and a cross-diffusion term, $\beta$ is a model coefficient, $f_\beta$ is a vortex-stretching modification factor, and $S_\omega$ is the user-specified source terms. The high-resolution interface capturing (HRIC) scheme [22] was used to discretize the transport equation for the volume fraction of water and air. The normalized variable diagram (NVD) [23] and normalized variables were used for the HRIC scheme. The normalized face value $\xi_f$ was calculated on the NVD using a combination of the upwind and downwind differencing schemes:

$$\xi_f = \begin{cases} \xi_C & if & \xi_C < 0 \\ 2\xi_C & if & 0 \le \xi_C < 0.5 \\ 1 & if & 0.5 \le \xi_C < 1 \\ \xi_C & if & 1 \le \xi_C \end{cases}, \tag{19}$$

where $\xi_C$ is the normalized cell value. The normalized face value is improved by considering the local value of the Courant number (CFL) $Co$:

$$Co = \frac{\boldsymbol{v}\boldsymbol{a}_f}{V_{P_C}}\Delta t, \tag{20}$$

where $\boldsymbol{a}_f$ is the face area, $\Delta t$ is the time step size, and $V_{P_C}$ is the control volume of the donor cell. A correction of the normalized face value $\xi_f^*$ was implemented to avoid stability problems during the simulations and to fulfill the convective boundedness criterion (CBC):

$$\xi_f^* = \begin{cases} \xi_C & if & Co < Co_l \\ \xi_C + \left(\xi_f - \xi_C\right)\frac{Co_u - Co}{Co_u - Co_l} & if & Co_l \le Co < Co_u \\ \xi_C & if & Co_u \le Co \end{cases}, \tag{21}$$

where $Co_l$ denotes the lower limit and $Co_u$ the upper limit for the CFL number. The HRIC scheme is used when CFL numbers are below $Co_l$. A blending of the HRIC scheme and the first-order upwind scheme (FOU) is used when CFL numbers are between $Co_l$ and $Co_u$. Only the FOU is used if the CFL number is greater than $Co_u$.

## 5. Numerical Setup

To reduce the computational domain from 12.53 to 4.53 m, longitudinal and vertical velocities and wave heights were pre-calculated for a longitudinal distance of 8.00 m from the wave maker. By incorporating a re-derived Boussinesq-type model [24] and implementing an advanced shoaling enhancement operator, an accurate distribution of vertical velocities was obtained that always satisfied the kinematic bottom boundary condition. An advanced potential formulation improved the effectiveness of the prior models [25–27] by converting the velocity formulation and, thus, enhancing the relation between both formulations.

The liquid phase of the two-phase flow was defined as incompressible water with a density of 1000 kg/m³, and the ambient air was assumed to be compressible.

The simulations discretized time implicitly to second-order, and a second-order scheme together with the mid-point rule discretized space. Initially, a flat wave defined the VoF wave model with a water height at 0.667 m. The multi-phase VoF model was used with the high-resolution interface capturing scheme (HRIC). A CFL of 0.5 specified the lower limit for the HRIC scheme, and a CFL of 1.0 as the upper limit. Use of a sharpening factor of 0.1 for the HRIC scheme [7] ensured obtaining accurate results. The surface average CFL number was kept below 0.2 during an entire simulation.

Seven prism layers surrounded the cylindrical structures. The specified thickness of the first prism layer ensured that all $y+$ values in the URANS simulations were below 3.0 and, on this basis, the physical area of the viscous sublayer was defined. As initial conditions, the static temperature of 293.15 K, the hydrostatic pressure of the flat VoF wave, and the zero velocity were defined. For the URANS simulations, the initial condition for the turbulent kinetic energy $k$ was 0.001 J/kg and, for the specific dissipation rate $\omega$, it was $1.0 \times 10^{-4}$ 1/s

The $x$-axis defined the length of the numerical canal; the $y$-axis, its width; and the $z$-axis, its height. The computational domain ranged from $x = 0$ m, defined as its inlet, to $x = 4.53$ m, defined as its back wall. The canal had a width of 0.65 m, ranging from $z = -0.669$ m to $z = 0.52$ m. The origin of the coordinate system was situated at the canal's centerline and the intersection of the undisturbed water level with the inlet. The cylinders in the first scenario as well as the cylinders in the second scenario and all walls, except the top wall, were defined as walls with the no-slip condition. The top wall was defined as a pressure outlet; one part of the inlet, as the velocity inlet; and the other part, as a wall.

Table 2 lists particulars describing the arrangement for the cylinders in the experimental setup, with the corresponding particulars describing the arrangement for the numerical setup in brackets. No brackets indicate that the arrangements in both setups were the same.

**Table 2.** Cylinder particulars describing the arrangement for the cylinders in the experimental setup and for the numerical setup (in brackets).

| | Cylinder Size | Length (m) | Diameter (m) | Longitudinal $\times$ Transversal $\times$ Vertical Position (m) | | | |
| --- | --- | --- | --- | --- | --- | --- | --- |
| | | | | Single Cylinder | | Upstream | Downstream |
| | | | | Low Position | High Position | Low Position | Low Position |
| Scenario 1 | Small | 0.8000 | 0.0889 | 11.62 (3.62) $\times$ 0 $\times$ −0.469—0.331 (−0.469—0.52) | 11.62 (3.62) $\times$ 0 $\times$ −0.269—0.531 (−0.269—0.52) | | |
| | Large | 0.8000 | 0.1524 | 11.62 (3.62) $\times$ 0 $\times$ −0.469—0.331 (−0.469—0.52) | 11.62 (3.62) $\times$ 0 $\times$ −0.269—0.531 (−0.269—0.52) | | |
| Scenario 2 | Medium | 0.8000 | 0.1230 | | | (3.374) $\times$ (0) $\times$ (−0.469—0.52) | (3.62) $\times$ (0.123) $\times$ (−0.469—0.52) |
| | Large | 0.8000 | 0.1524 | | | (3.3152) $\times$ (0) $\times$ (−0.469—0.52) | (3.62) $\times$ (0.1524) $\times$ (−0.469—0.52) |

For 434 heights along the $z$-axis, two distinct files stored the local vertical and horizontal velocities and the wave elevation at the inlet. This length extended from $z = -0.667$ m to $z = 0.199$ m, and a distance of 0.002 m separated these incremental heights from each other. A total of 434 blocks were created to allocate the data to the velocity inlet. The first block had a height of 0.001 m and comprised data for the first point. The following blocks had a height of 0.002 m and consisted of data of the remaining 433 points. The rest of the inlet, extending from $z = 0.2$ m to $z = 0.52$ m, was defined as a wall with the no-slip condition.

To validate the numerical method, predicted impact forces acting on the single large cylinder were compared with experimentally measured impact loads. Some simulations implemented the laminar flow model and others the turbulent flow model. Two sets of three successively finer grids were generated on which to compute the simulations. The refinement ratio of $\sqrt{2}$ was applied for the spatial as well as the time step sizes to ensure obtaining the same Courant number for each grid. Table 3 lists the number of cells and the associated time step sizes of the coarse, medium, and fine grid.

The cells of all grids were hexahedral, and each cell was aligned at the origin of its coordinate system located at the intersection between the gaseous and the liquid phase. As a result, all cells contained either 100% of the gaseous phase or 100% of the liquid phase at the beginning of the simulation. Thus, at the start no unintentional mixing of the individual phases occurred.

**Table 3.** Number of cells (CVs) and time steps sizes of grids used to validate the numerical method. Data from [11].

| | Coarse Grid (1,085,131 CVs) | | Medium Grid (2,829,244 CVs) | | Fine Grid (7,519,511 CVs) | |
|---|---|---|---|---|---|---|
| | Time Step (Start) (s) | Time Step (s) | Time Step (Start) (s) | Time Step (s) | Time Step (Start) (s) | Time Step (s) |
| Set 1 | $8 \times 10^{-3}$ | $2 \times 10^{-3}$ | $5.657 \times 10^{-3}$ | $1.414 \times 10^{-3}$ | $4 \times 10^{-3}$ | $1 \times 10^{-3}$ |
| Set 2 | $5.657 \times 10^{-3}$ | $1.414 \times 10^{-3}$ | $4 \times 10^{-3}$ | $1 \times 10^{-3}$ | $2.828 \times 10^{-3}$ | $7.071 \times 10^{-4}$ |

Grids were refined in the vicinity of the free surface, ranging from $z = -0.10$ to 0.20 m, and at the cylinder to dissolve the wave shape and the higher velocities more accurately and to prevent unwanted vortices forming at the cylinders. Cell lengths were 0.0125 m for the coarse grid, 0.00884 m for the medium grid, and 0.00625 m for the fine grid. For the remaining area, the cell length was 0.025 m for the coarse grid, 0.01768 m for the medium grid, and 0.0125 m for the fine grid. The cell length in the vicinity of the cylinder was 0.00625 m for the coarse grid, 0.00442 m for the medium grid, and 0.003125 m for the fine grid. The total thickness of the prism layer was 0.00532 m for the coarse grid, 0.00376 m for the medium grid, and 0.00266 m for the fine grid, whereas the thickness of the first prism layer was $0.031 \times 10^{-3}$ m for all grids. Figure 1 shows a side view and Figure 2 a top view of the grids (at $z = 0$ m) surrounding the large cylinder.
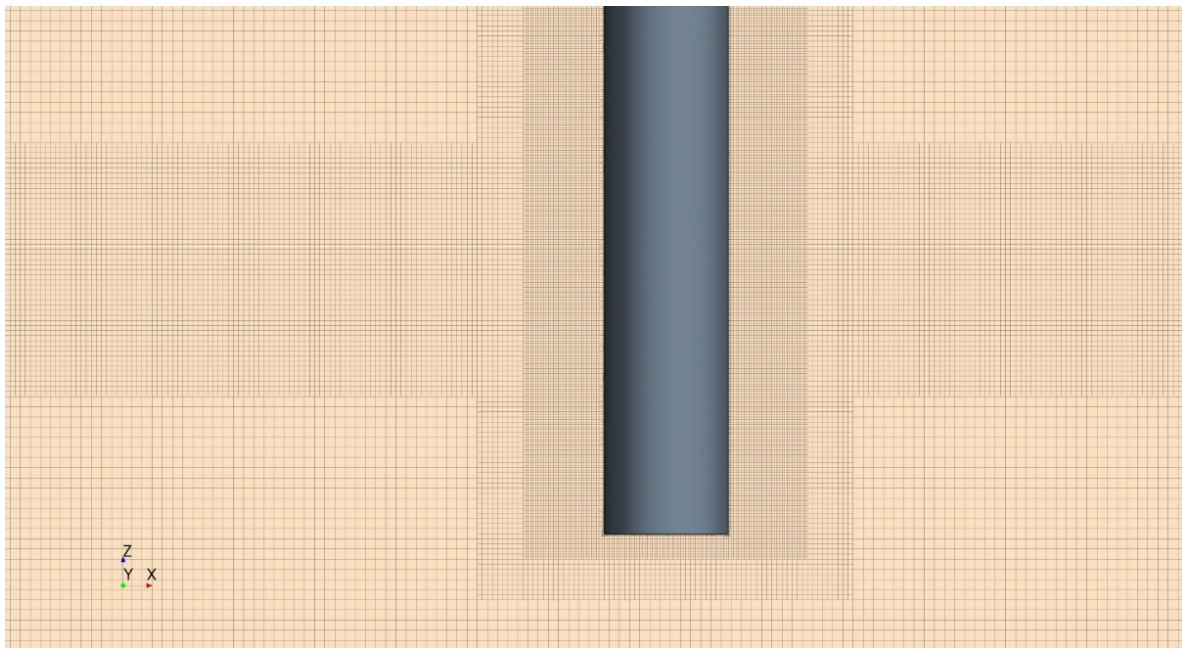


**Figure 1.** Side view of grid refinement in the vicinity of the large cylinder and at the free surface.

The simulations for the second scenario were obtained only with the implemented turbulent model. The time step size and basic grid structure were based on results from our previous validation study [11] and adapted for the tripod configuration. A prism layer thickness of 0.00266 m was defined for the large-sized cylinders and 0.00215 m for the medium-sized cylinders. The thickness of the first prism layer was $0.031 \times 10^{-3}$ m for the large cylinders and $0.03 \times 10^{-3}$ m for the medium-sized cylinders, thereby obtaining the same low wall $y+$ number. Seven prism layers were considered. The cells surrounding the upstream and downstream cylinders were 0.003125 m long, which enabled to accurately capture the turbulent flow in the area between the cylinders and, therefore, to account for the vortex-induced interaction between the cylinders. To evaluate the effectiveness of the Morison equation, the cylinders were removed from the numerical canal, and the velocities

and accelerations were gathered at the positions of the removed cylinders. Figure 3 depicts a top view of grid refinement in the vicinity of the three large cylinders at the height of *z* = 0 m. Table 4 lists particulars for the numerical cases.
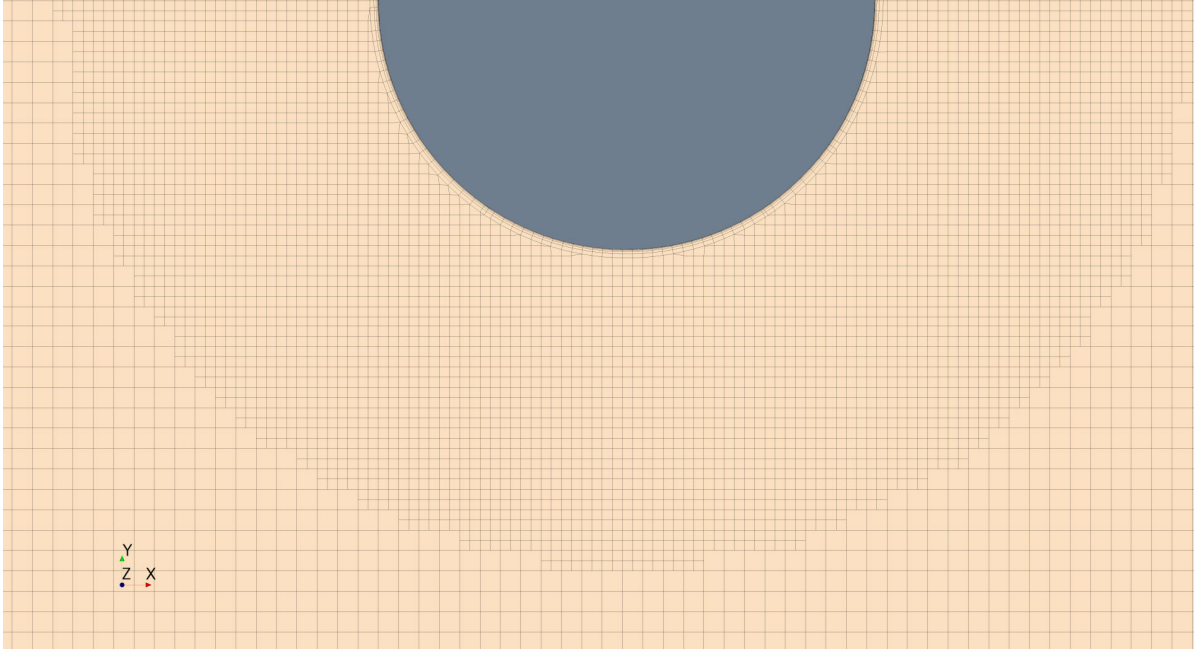


**Figure 2.** Top view of one half of the grid refinement in the vicinity of the large cylinder at *z* = 0 m.
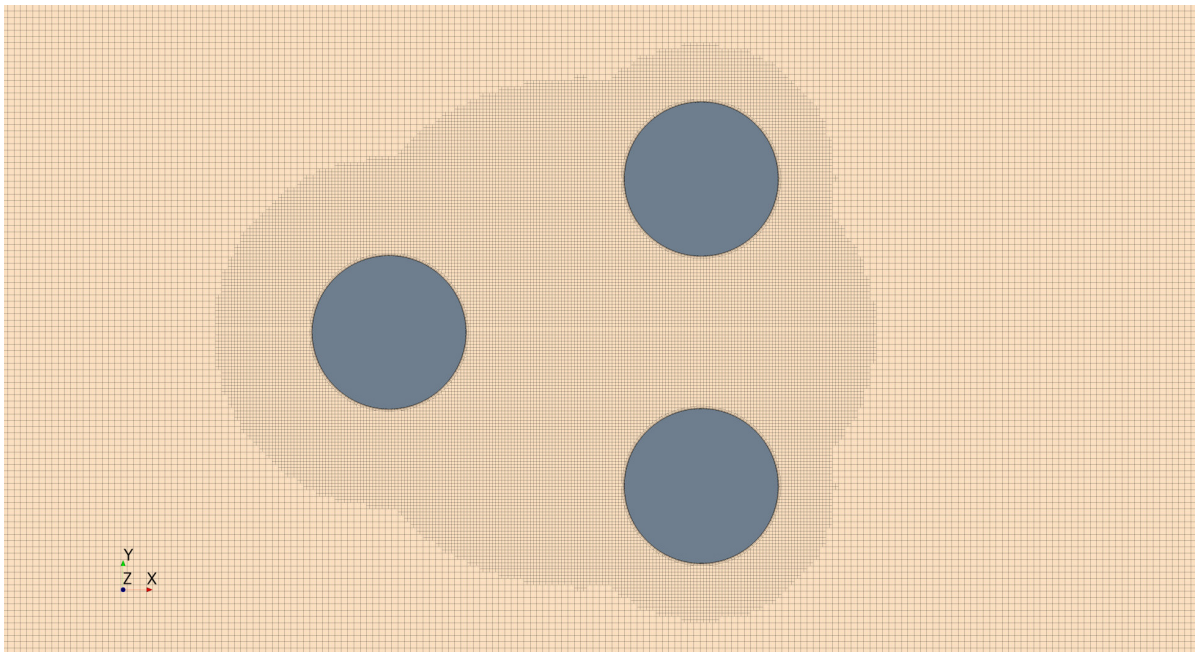


**Figure 3.** Top view of grid refinement in the vicinity of the large cylinders in the tripod configuration at *z* = 0 m.

**Table 4.** Overview of the numerical cases.

| | Flow Model | Cylinder Sizes | Quantity of Simulations | Cylinder Immersion during Validation Study (m) | Cylinder Immersion after Validation Study (m) | |
|---|---|---|---|---|---|---|
| | | | | Low Position | High Position | Low Position |
| Scenario 1 | Laminar | Large | 6 (3 each with Set 1 and Set 2) | −0.469 | | |
| | Turbulent | Small | 4 (2 each with Morison and URANS for both positions) | | −0.269 | −0.469 |
| | Turbulent | Large | 6 (3 each with Set 1 and Set 2) for low position; 4 (2 each with Morison and URANS for both positions) | −0.469 | −0.269 | −0.469 |
| Scenario 2 | Turbulent | Medium | 6 (2 each with Morison and URANS for all three cylinders) | | | −0.469 |
| | Turbulent | Large | 6 (2 each with Morison and URANS for all three cylinders) | | | −0.469 |

## 6. Validation

Two simulations were conducted per grid with the turbulence model and two simulations per grid with the laminar model. Set 1 comprised simulations with the larger time steps and set two simulations with the finer time step, see Table 3. Thus, the CFL number differed only between the two sets and remained the same within each set. The least squares method [28] was used to obtain grid and time step independent solutions for a constant CFL number [29].

The two top graphs of Figure 4 plot time histories of the longitudinal load, based on the laminar flow model, acting on the large cylinder obtained on the three grids of set 1 and set 2. The black line depicts experimentally measured loads; the yellow line, loads computed on the coarse grid; the red line, loads computed on the medium grid; the blue line, loads computed on the fine grid. To better distinguish differences between peak load predictions, the two bottom graphs of Figure 4 present zoomed views of these time histories representing time intervals within the small rectangular box in the top graphs of Figure 4. As seen, for both sets the predicted load obtained on the coarse grids came closest to the measured load. Furthermore, with increasing grid fineness computed loads increased and deviated more from the measured loads.

The upper graph of Figure 5 plots time step refinement ratio versus grid spacing refinement ratio for simulations based on the laminar model. This grid spacing refinement ratio $x_{ij}$ is defined as follows:

$$x_{ij} = \frac{Spacing_{grid_i\_set_j}}{Spacing_{grid_1\_set_1}},$$  (22)

where indexes $i$ = 1, 2, 3 refer to the coarse, the medium, and fine grids, respectively, and indexes $j$ = 1 and 2 refer to sets 1 and 2, respectively. The time step refinement ratio $y_{ij}$ is defined as follows:

$$y_{ij} = \frac{t_{grid_{i}\_set_{j}}}{t_{grid_{1}\_set_{1}}},$$

(23)

where $t$ represents the time step, indexes $i = 1, 2, 3$ refer to the coarse, the medium, and fine grids, respectively, and indexes $j = 1$ and $2$ refer to sets 1 and 2, respectively. The denominator of this ratio is always the largest time step, i.e., the time step of grid 1 in set 1.
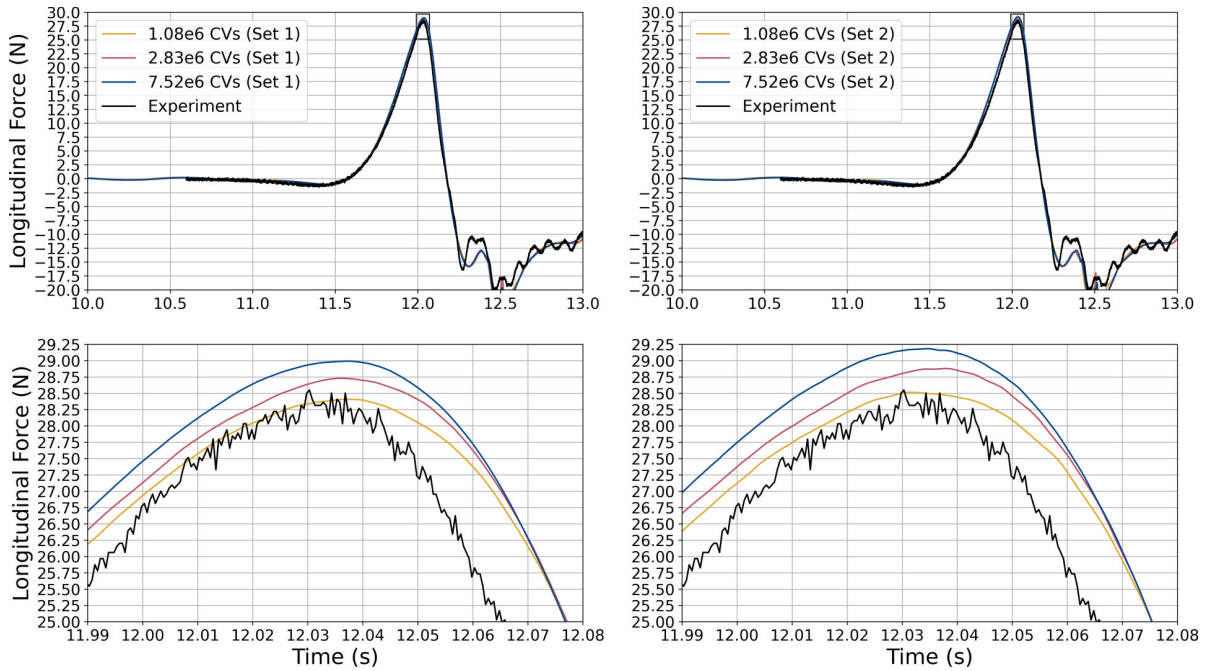


**Figure 4.** Time histories of wave-induced loads acting on the large cylinder obtained on the three grids of set 1 (**top left**) and set 2 (**top right**) and zoomed views of the associated load peaks of set 1 (**bottom left**) and set 2 (**bottom right**) based on the laminar flow model.
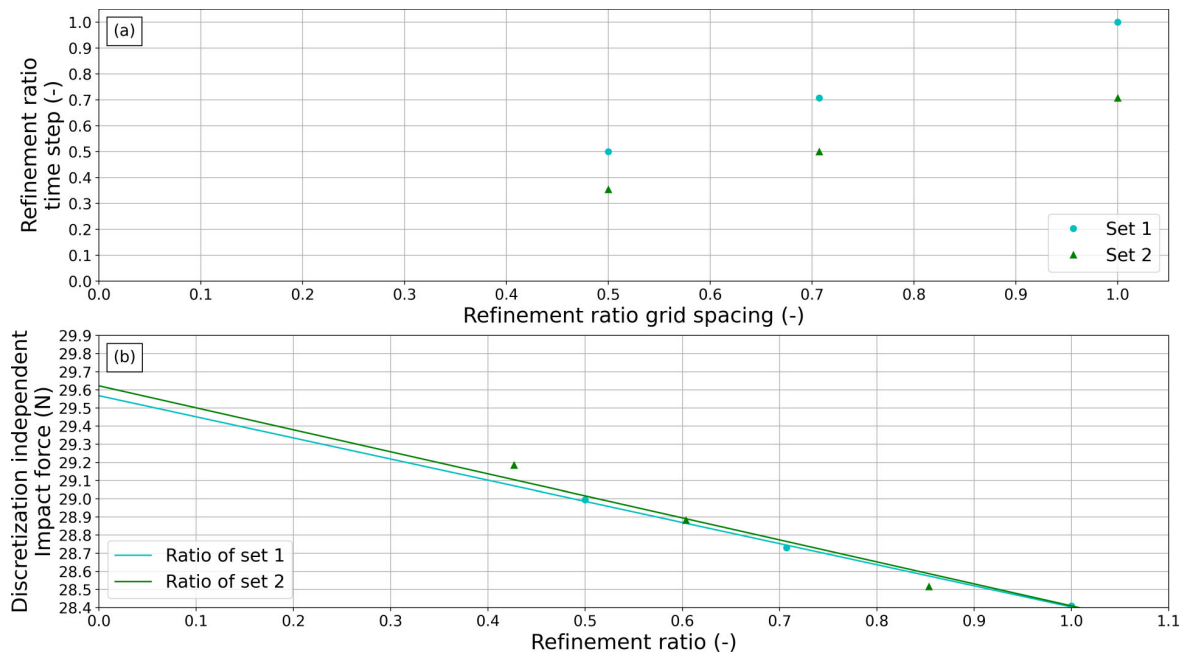


**Figure 5.** Time step refinement ratio versus grid spacing refinement ratio (**a**) and grid spacing and time step independent longitudinal impact load versus the arithmetic mean of the $x_{ij}$ and $y_{ij}$ (**b**) based on the laminar flow model.

The number of control volumes remained the same for set 1 and set 2. Thus, the grid spacing differed only between the coarse, the medium, and the fine grid. Recall that the refinement factor of $\sqrt{2}$ was the same for the grid spacing and the time step size.

The lower graph of Figure 5 plots the grid spacing and time step independent longitudinal impact load versus the arithmetic mean $X_{ij}$ of $x_{ij}$ and $y_{ij}$ defined as follows:

$$X_{ij} = \frac{x_{ij} + y_{ij}}{2}, \tag{24}$$

The cyan line represents the time step and grid independent solution for the impact load in set 1; the green line, the time step and grid independent solution for the impact load in set 2. Sets 1 and 2 yielded the impact loads of 29.57 N and 29.62 N, respectively, and the experimentally measured impact load was about 28.55 N. Thus, the numerically computed impact load deviated by about 3.6% from the measured impact. Recall that these load computations were based on the laminar flow model.

The two top graphs of Figure 6 plot time histories of the longitudinal load, here based on the turbulent flow model, acting on the large cylinder obtained on the three grids of set 1 and set 2. As in Figure 4, the black line depicts experimentally measured loads; the yellow line, loads computed on the coarse grid; the red line, loads computed on the medium grid; the blue line, loads computed on the fine grid. Here, too, the two bottom graphs of Figure 6 present zoomed views of these time histories representing time intervals within the small rectangular box in the top graphs of Figure 6. As seen, the predicted impact load obtained on the finest grid in set 2 compared best to the experimentally measured impact load.
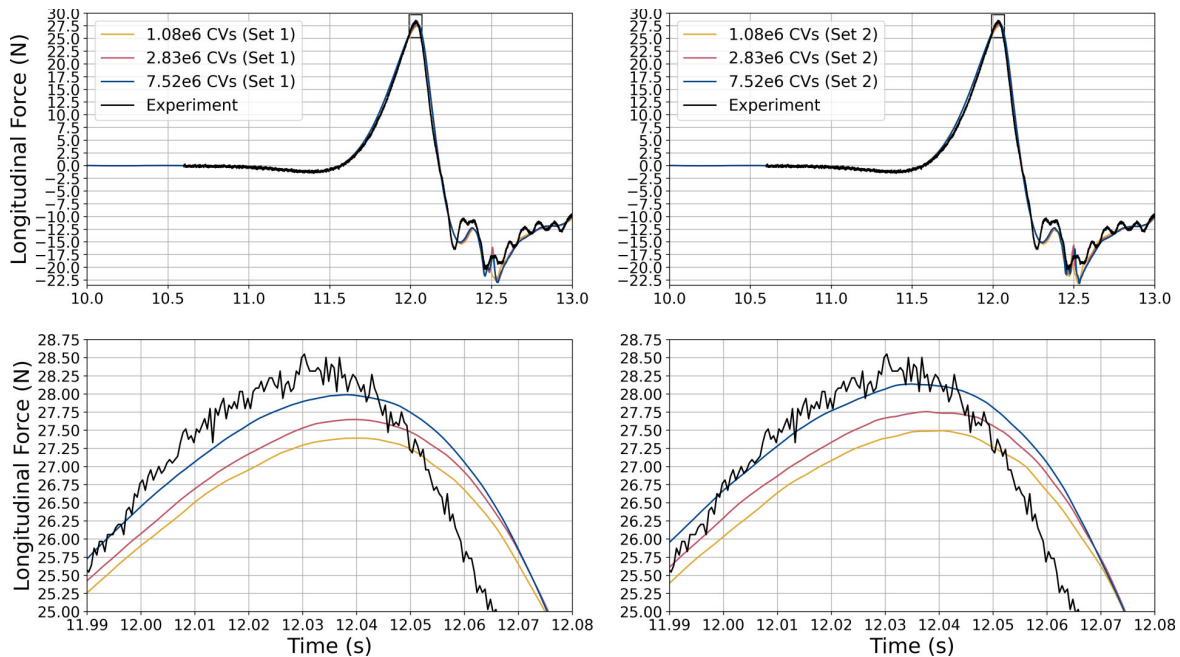


**Figure 6.** Time histories of wave-induced loads acting on the large cylinder obtained on the three grids of set 1 (**top left**) and set 2 (**top right**) and zoomed views of the associated load peaks of set 1 (**bottom left**) and set 2 (**bottom right**) based on the turbulent flow model. The data were from ref. [11].

Sets 1 and 2 yielded the discretization independent impact loads of 28.54 N and 28.52 N, respectively, see Figure 7. The favorable agreement between the measured impact load of 28.55 N and the discretization independent impact loads in both sets indicated that the computations were able to yield reliably predictions. Table 5 summarizes these results and lists the calculated and measured value for the impact loads and the deviation between both. Recall that these load computations were based on the turbulent flow model.
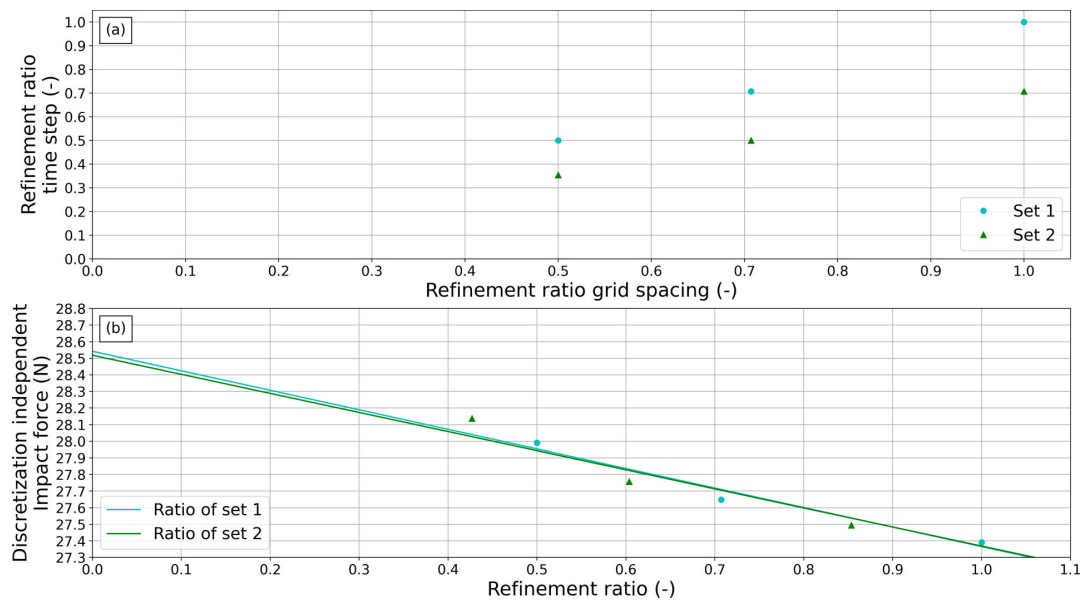
**Figure 7.** Time step refinement ratio versus grid spacing refinement ratio (**a**) and grid spacing and time step independent longitudinal impact load versus the arithmetic mean of the $x_{ij}$ and $y_{ij}$ (**b**) based on the turbulent flow model. The data were from ref. [11].

**Table 5.** Discretization-independent predictions and impact loads from the coarse, medium, and fine grids and their deviations from experimental measurements (in brackets).

| | Coarse Grid Impact (N) and Deviation from Experiments (%) | | Medium Grid Impact (N) and Deviation from Experiments (%) | | Fine Grid Impact (N) and Deviation from Experiments (%) | | Discretization Independent Impact (N) and Deviation from Experiments (%) | |
|---|---|---|---|---|---|---|---|---|
| | Laminar | (SST) k–ω | Laminar | (SST) k–ω | Laminar | (SST) k–ω | Laminar | (SST) k–ω |
| Set 1 | 28.41 (0.49) | 27.39 (4.06) | 28.73 (0.63) | 27.65 (3.15) | 28.98 (1.51) | 27.99 (1.96) | 29.57 (3.57) | 28.54 (0.035) |
| Set 2 | 28.51 (0.14) | 27.49 (3.71) | 28.88 (1.16) | 27.76 (2.78) | 29.18 (2.21) | 28.14 (1.44) | 29.62 (3.75) | 28.52 (0.11) |

These uncertainty studies demonstrated that loads based on the turbulent flow model yielded more accurate and higher predictions than those based on the laminar flow model. Therefore, subsequent computations were carried out with the turbulence model on the finest grid with the time step for set 2. Of course, the grid was adapted for the differently sized cylinders and the tripod configuration accordingly.

## 7. Comparison of Load Coefficients for Single Cylinder and Cylinders in the Tripod Configuration Considering the Influence of Wake Effects

In the first scenario, longitudinal flow velocities were pre-calculated at 210 points along the *z*-axis located at the single cylinder's longitudinal position of $x = 3.62$ m. These probe points, separated by 0.0032 m from each other, extended from $z = -0.4674$ m to $z = 0.2014$ m. The length per segment $dS$, therefore, was 0.0032 m for a cylinder immersed to a depth of $z = -0.4690$ m.

However, for a cylinder immersed to a depth of $z = -0.2690$ m, the pre-calculation of flow velocities started at the 64th probe point located at $z = -0.2658$ m. To avoid repeating the simulation with different positions of the probe points, the segment length $dS$ was increased to 0.0064 m. Thus, flow velocities were obtained at every second probe point for this cylinder. Figure 8 shows the arrangement and location of the single cylinder in this first scenario and the 210 probe points at which the longitudinal velocities were pre-calculated. For illustrative purposes, only 22 of the 210 probes are shown in Figure 8.
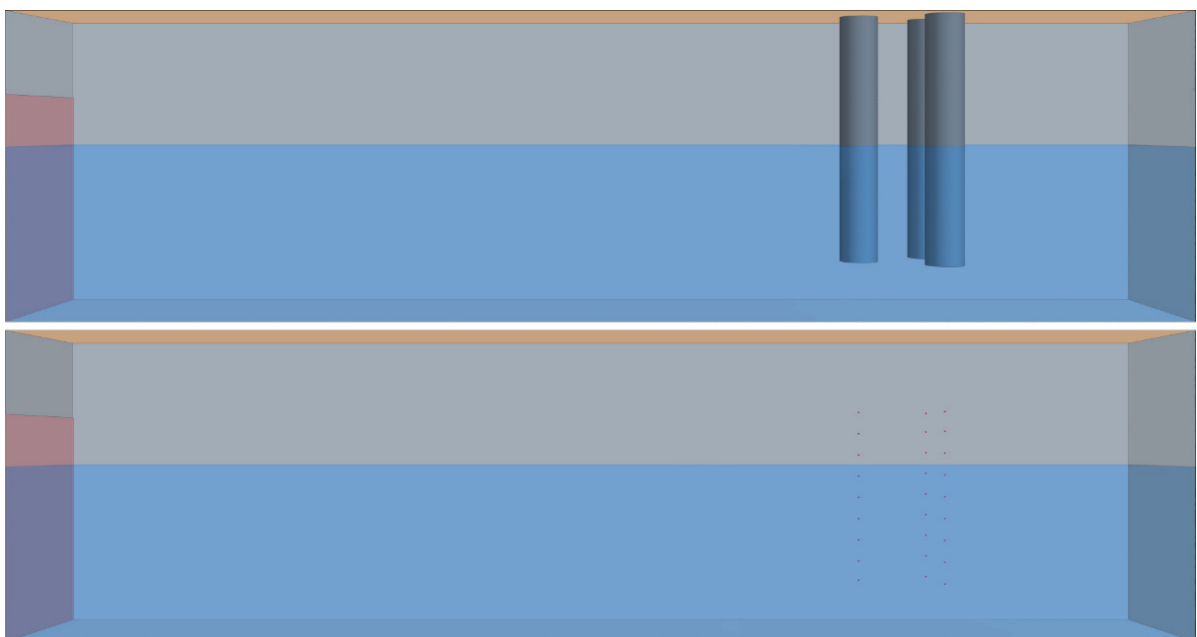
**Figure 8.** Arrangement of a single cylinder in the first scenario (**top**) and the 210 probe points (only 22 in this figure for illustrative purposes) at which longitudinal velocities were pre-calculated (**bottom**).

In the second scenario, velocities were obtained at 80 probe points along the $z$-axis located at the three cylinders' longitudinal positions, i.e., at a total of 240 probe points. These probe points were separated by a distance of 0.0086 m from each other and extended from $z = -0.4647$ m to $z = 0.2147$ m. The cylinders were immersed to a depth of $z = -0.4690$ m. Figure 9 shows the arrangements of the three cylinders for the tripod configuration in the second scenario and the 240 probe points at which longitudinal velocities were pre-calculated. For illustrative purposes, only 27 of the 240 probes are shown in Figure 9.



**Figure 9.** Arrangement of the three cylinders for the tripod configuration in the second scenario (**top**) and the 240 vertical probe points (only 27 in this figure for illustrative purposes) at which longitudinal velocities were pre-calculated (**bottom**).

Figure 10 plots time histories of the temporal waveform at the longitudinal positions of the single cylinders and of the downstream cylinders, which is located at $x$ = 3.62 m, of the medium-sized upstream cylinder, which is located at $x$ = 3.374 m and of the large-sized upstream cylinder, which is located at $x$ = 3.3152 m.
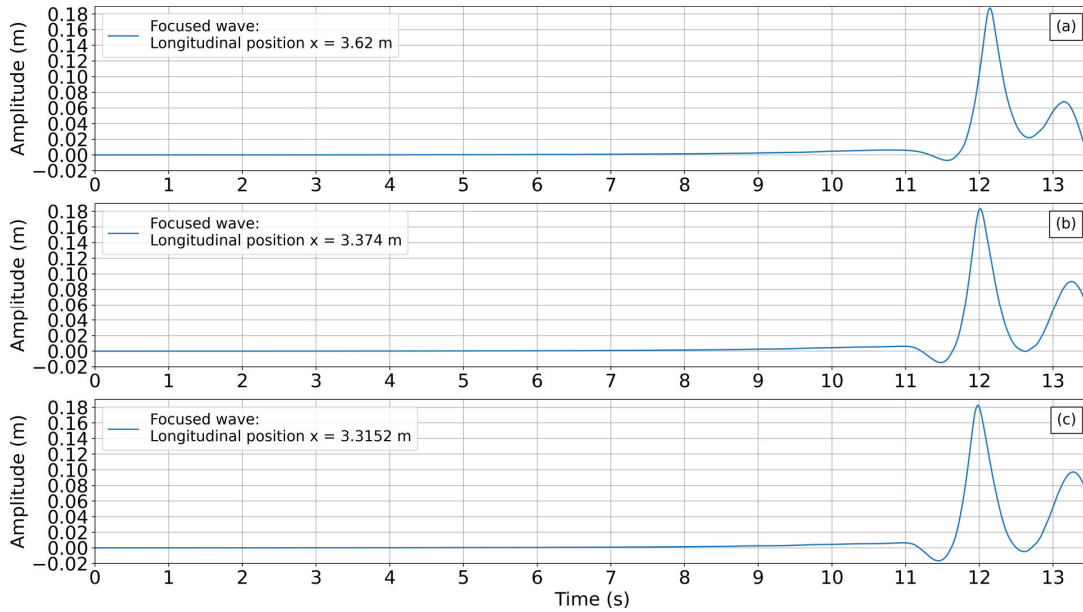


**Figure 10.** Temporal waveform of the focused wave at the longitudinal locations of (**a**) $x$ = 3.62 m, (**b**) $x$ = 3.374 m and (**c**) $x$ = 3.3152 m.

Figure 11a plots time histories of pre-calculated flow velocities at the probe points in the first scenario for the single cylinder immersed to a depth of $z$ = −0.4690 m; and Figure 11b for the single cylinder immersed to a depth of $z$ = −0.2690 m. A color bar indicates the vertical position of the probe points.
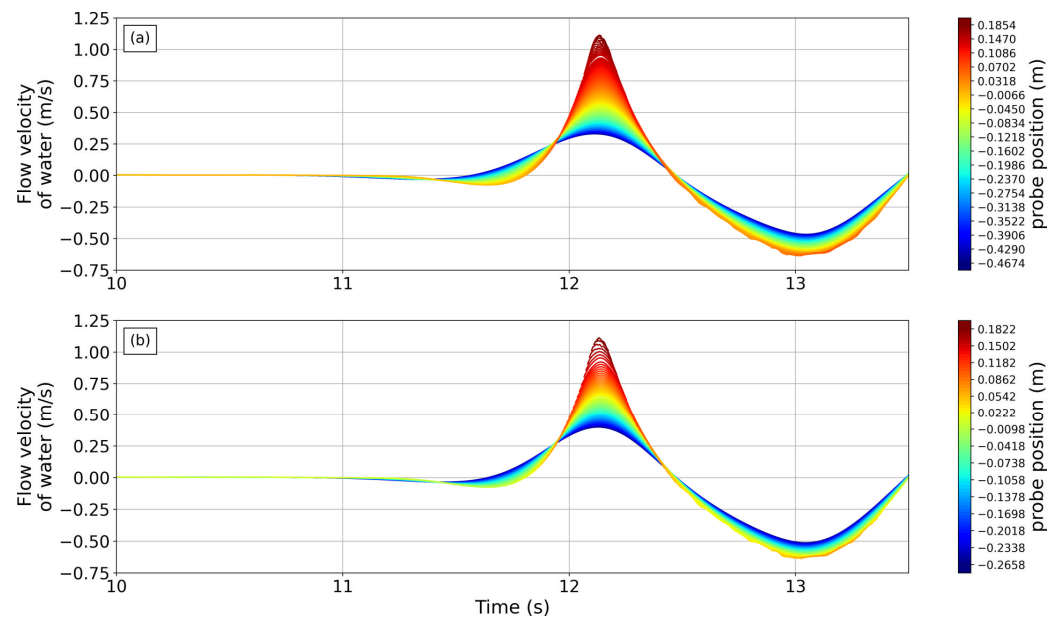


**Figure 11.** Time histories of pre-calculated flow velocities at probe points in the first scenario for the single cylinder immersed to a depth of $z$ = −0.4690 m (**a**) and to a depth of $z$ = −0.2690 m (**b**). The color bar indicates the vertical position of the probe points.

Figures 12 and 13 plot time histories of pre-calculated flow velocities for the tripod configuration considered in the second scenario. The time histories in Figure 12 refer to the configuration consisting of the large-diameter cylinders; the time histories in Figure 13, to the configuration consisting of the medium-diameter cylinders. Graph (a) of Figures 12 and 13 refers to flow velocities at the upstream cylinder; Graph (b) refers to flow velocities at the starboard downstream cylinder; Graph (c) refers to flow velocities at the portside downstream cylinder.
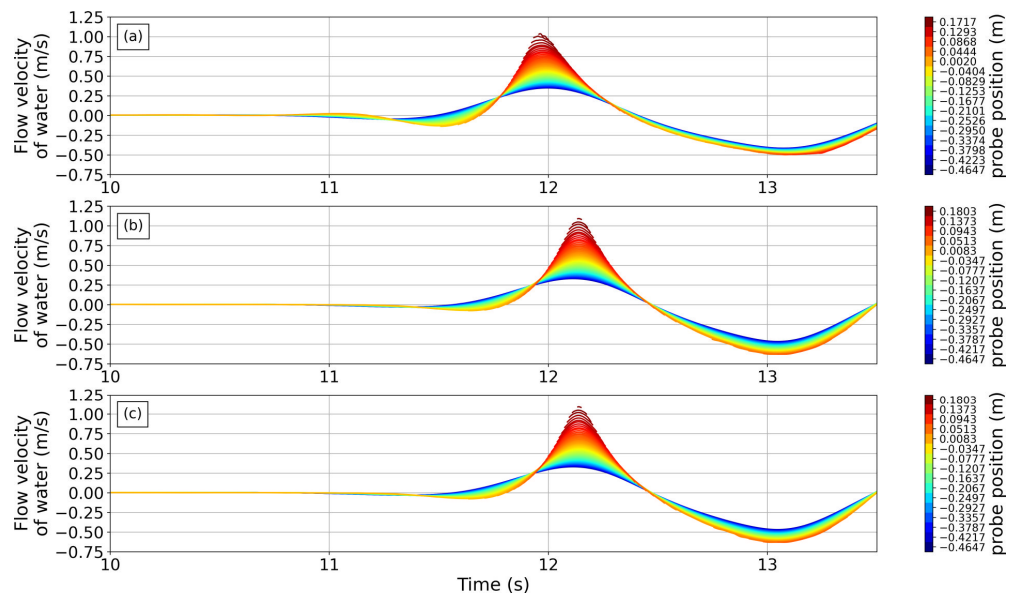


**Figure 12.** Time histories of flow velocities at probe points in the second scenario at the upstream cylinder (**a**), at the downstream starboard cylinder (**b**), and at the downstream portside cylinder (**c**) for the tripod configuration consisting of large-diameter cylinders. The color bar indicates the vertical position of the probe points.
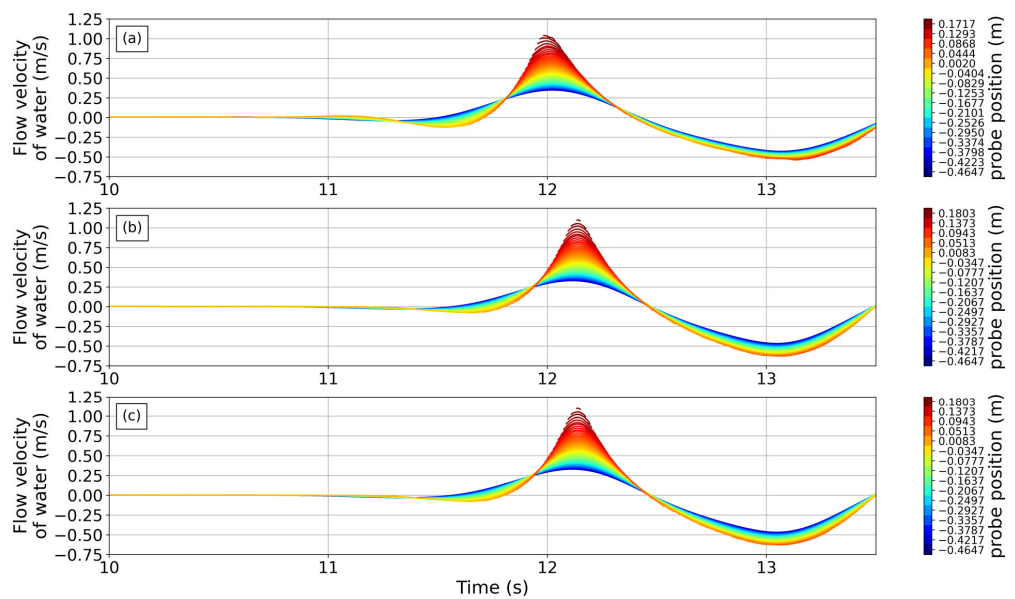


**Figure 13.** Time histories of flow velocities at probe points in the second scenario at the upstream cylinder (**a**), at the downstream starboard cylinder (**b**), and at the downstream portside cylinder (**c**) for the tripod configuration consisting of medium-diameter cylinders. The color bar indicates the vertical position of the probe points.

The times between maximum and minimum flow velocity in Figures 11–13 were multiplied by a factor of two, and these times were treated as a wave period of the focused wave representing the period of a sloshing motion acting on a single vertical cylinder or on a typical tripod configuration of a pump tower. A previous investigation of ours demonstrated that this approach yielded practically relevant estimates [11].

To establish load coefficients, the wave period needed to be specified as this enabled determining Sarpkaya's beta factor $\beta$ [3]:

$$\beta = \frac{D^2}{\vartheta T_m}, \tag{25}$$

where $\vartheta$ is the kinematic viscosity, and $T_m$ is the wave period. Sarpkaya defined drag coefficients $C_D$ and inertia coefficients $C_M$ as a function of the Keulegan and Carpenter parameter $K_C$ [2]:

$$K_C = \frac{U_m T_m}{D}, \tag{26}$$

where $U_m$ is the oscillating flow's maximum velocity at the point where the load is acting, that is, at the probe points in our case.

In the first scenario, the wave period 1.87 s and the maximum velocity were the same for all simulations because the location of the probe points along the single cylinder did not change. In the second scenario, the longitudinal position of the upstream cylinder differed from that of the downstream cylinders and, thus, the wave period was modified. While the wave period for the downstream cylinders remained at about 1.87 s in all simulations, the modified wave period was 2.32 s for the large-diameter upstream cylinder and 2.29 s for the medium-diameter upstream cylinder.

In the first scenario, the $\beta$ parameter turned out to be 12,383 for the large-diameter cylinder and 4214 for the small-diameter cylinder, and the $K_C$ parameter was 13.7 for the large-diameter cylinder and 23.4 for the small-diameter cylinder.

In the second scenario's configuration with the medium-diameter cylinders, $\beta$ and $K_C$ were 6587 and 19.6, respectively, for the upstream cylinder, and 8066 and 16.7, respectively, for the downstream cylinders.

In the second scenario's configuration with the large-diameter cylinders, $\beta$ and $K_C$ were 9981 and 15.9, respectively, for the upstream cylinder and 12,383 and 13.7, respectively, for the downstream cylinders.

Sarpkaya performed experimental tests for $\beta$ values of 4480, 6555, 8370, and 11,525 [3,30]. From his tests for $\beta = 4480$, drag and inertia coefficients were extracted for the small-diameter cylinder in the first scenario; from his tests for $\beta = 6555$, drag and inertia coefficients were extracted for the upstream cylinder in the configuration with the medium-diameter cylinders; from his tests for $\beta = 8370$, drag and inertia coefficients were extracted for the downstream cylinders in the configuration with the medium-diameter cylinders, and from his tests for $\beta = 11,525$, drag and inertia coefficients were extracted for the large cylinder in the first scenario and the upstream and downstream cylinders in the configuration with the large-diameter cylinders. Table 6 lists these extracted drag and inertia coefficients as well as the associated wave periods and $\beta$ and $K_C$ values.

To compare the predicted hydrodynamic loads against experimental measurements, the coefficient $c_x$ was introduced, which expresses the normalized loads as follows [7]:

$$c_x = \frac{F}{\rho \cdot \left(2\pi^2 \cdot \frac{1}{T_p^2} \cdot A_w^2\right) \cdot A_{Area}}, \tag{27}$$

where $F$ represents the hydrodynamic load, $T_P$ the peak period, $A_w$ the maximum wave height of the respective focused wave, and $A_{Area}$ the surface area of the cylinder.

**Table 6.** Wave periods, $\beta$ and $K_C$ values, and extracted drag and inertia coefficients for the first and second scenarios.

| Scenario | Cylinder Size | Cylinder Position | $T_m$ (s) | $\beta$ | $K_C$ (-) | $C_D$ (-) | $C_M$ (-) |
|----------|---------------|-------------------|-----------|---------|-----------|-----------|-----------|
| 1 | Small | | 1.87 | 4214 | 23.4 | 0.66 | 1.7 |
| | Large | | 1.87 | 12,383 | 13.7 | 0.68 | 1.77 |
| 2 | Medium | Upstream | 2.29 | 6587 | 19.6 | 0.684 | 1.714 |
| | | Downstream | 1.87 | 8066 | 16.7 | 0.65 | 1.79 |
| | Large | Upstream | 2.32 | 9981 | 15.9 | 0.71 | 1.68 |
| | | Downstream | 1.87 | 12,383 | 13.7 | 0.68 | 1.77 |

Figure 14 presents comparative time histories of load coefficient $c_x$ for the low- and high-positioned cylinder in the first scenario. A black line identifies $c_x$ values based on experimentally measured loads; a dark red line, $c_x$ values based on URANS computed loads; an indigo line, $c_x$ values based on loads calculated with the Morison equation. Figure 14a,c of this figure refer to loads acting on the small-diameter cylinder in its low and high positions, respectively; Figure 14b,d of this figure refer to loads acting on the large-diameter cylinder in its low and high positions, respectively.
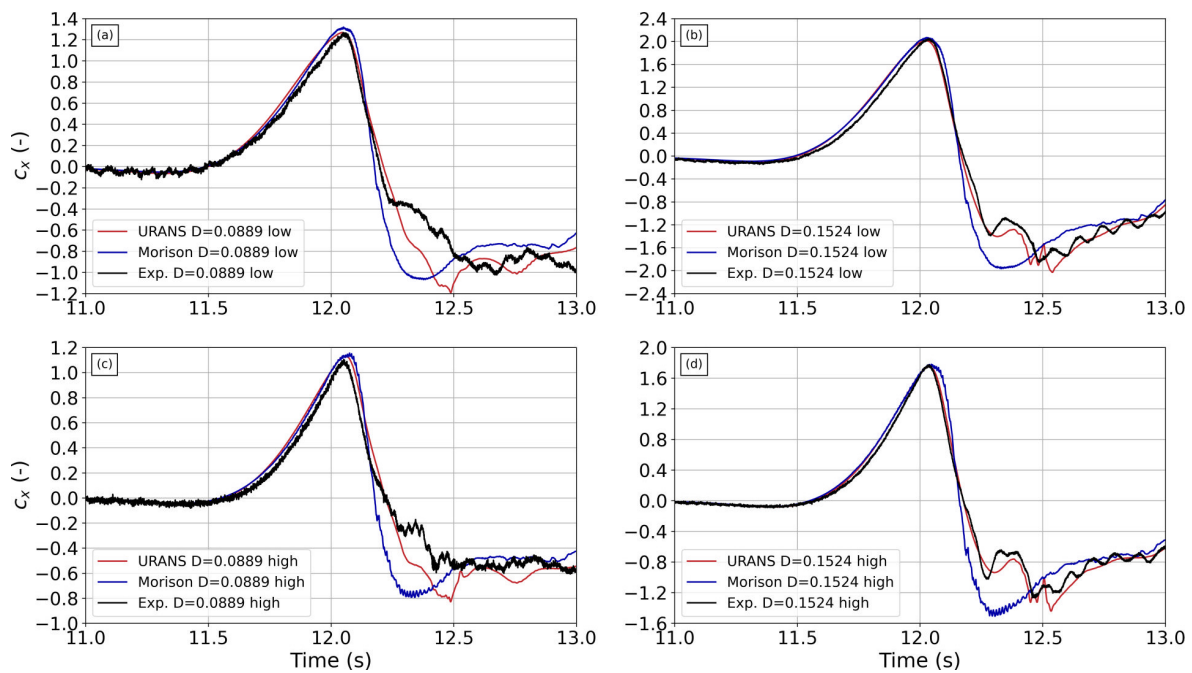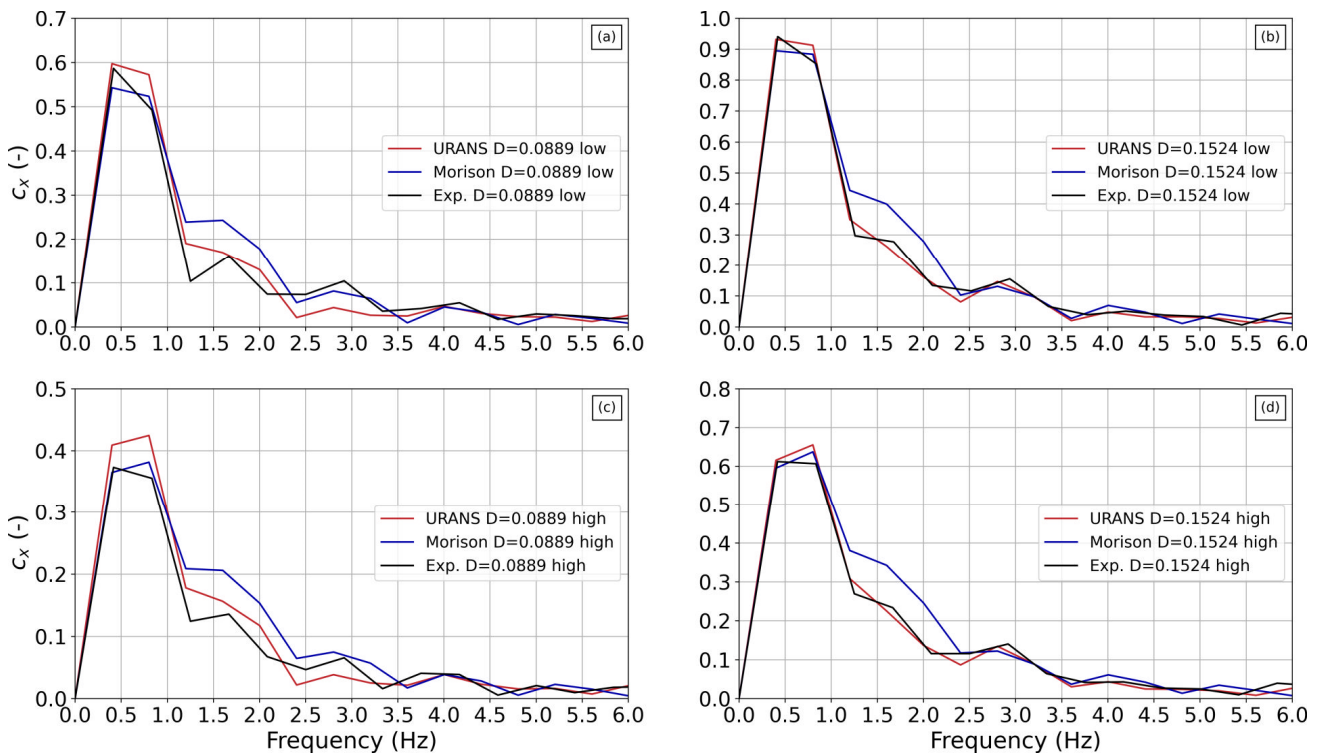


**Figure 14.** Time histories of load coefficient $c_x$ in scenario 1 for the small-diameter cylinder in its low position (**a**), for the large-diameter cylinder in its low position (**b**), for the small-diameter cylinder in its high position (**c**), and for the large-diameter cylinder in its high position (**d**).

Generally, in all four cases the computed and calculated loads compared favorably to measurements, especially in the vicinity of the impacting load peaks. However, after impact, predicted loads differed somewhat from measurements although the URANS computed loads acting on the large-diameter cylinder agreed fairly well with measurements. Nevertheless, for the small-diameter cylinder, the Morison equation yielded loads that closely matched the URANS computed loads even after impact. After impact, not only the URANS simulations, but also the Morison equation based solutions had difficulties reproducing the temporal progression. This could have been due to the reduced stiffness of the small-diameter cylinder.

Figure 15 presents the comparative frequency spectra of load coefficient $c_x$, derived via a fast Fourier transform (FFT), for the low- and high-positioned cylinder in the first scenario. Again, a black line identifies $c_x$ values based on experimentally measured loads; a dark red line, $c_x$ values based on URANS computed loads; an indigo line, $c_x$ values based on loads calculated with the Morison equation. Figure 15a,c of this figure refer to loads acting on the small-diameter cylinder in its low and high positions, respectively; Figure 15b,d of this figure refer to loads acting on the large-diameter cylinder in its low and high positions, respectively.



**Figure 15.** Frequency spectra of load coefficient $c_x$ in scenario 1 for the small-diameter cylinder in its low position (**a**), for the large-diameter cylinder in its low position (**b**), for the small-diameter cylinder in its high position (**c**), and for the large-diameter cylinder in its high position (**d**).

The URANS computed load coefficients and experimental measurements compared favorably for the large-diameter cylinder in its low position. There were two visible peaks at about 0.5 Hz and 3 Hz. Although load coefficients based on the Morison equation were somewhat lower than measured coefficients, they had two peaks at these same frequencies. The same tendency was observed for the small-diameter cylinder in its low position at the first peak. Four peaks characterized the spectrum of the load coefficient based on experimental measurements. Load coefficients from URANS computations and from the Morison equation yielded three visible peaks. The second and third peaks were at the same frequency as the third and fourth peaks of the coefficients based on experiments although the experimentally based peaks were slightly larger. The number of peaks and their occurrence frequency were nearly the same for the small-diameter cylinder in its high position. The URANS based coefficients were higher at the first peaks. Load coefficients based on experiments and on the Morison equation matched favorably at the first peak. Coefficients for the large-diameter cylinder in its high position compared favorably to both coefficients based on predictions and measurements. The frequency of the first peak shifted slightly to a higher value for the large-diameter cylinder in its low position.

Figure 16 presents comparative time histories of load coefficients for the medium-diameter cylinders in their tripod configuration, i.e., in the second scenario. The dark red line identifies the URANS computed coefficients and the indigo line, the coefficients

calculated with the Morison equation. These identifications apply also to the Figures 17–19. Graphs (a) of these figures refer to coefficients for the upstream cylinder; Graphs (b) refer to coefficients for the downstream starboard cylinder; Graphs (c) refer to coefficients for the downstream portside cylinder. For the upstream cylinder, the impact from the Morison equation was slightly higher than the impact from for URANS computation; however, for both downstream cylinders, the impact from the Morison equation was slightly lower than the impact from the URANS computation. For the upstream cylinder, the temporal progression of load coefficients obtained from both methods agreed better than for the two downstream cylinders. The wake effect from the upstream cylinder could not be captured by the Morison equation because the upstream cylinder was not accounted for in these computations.
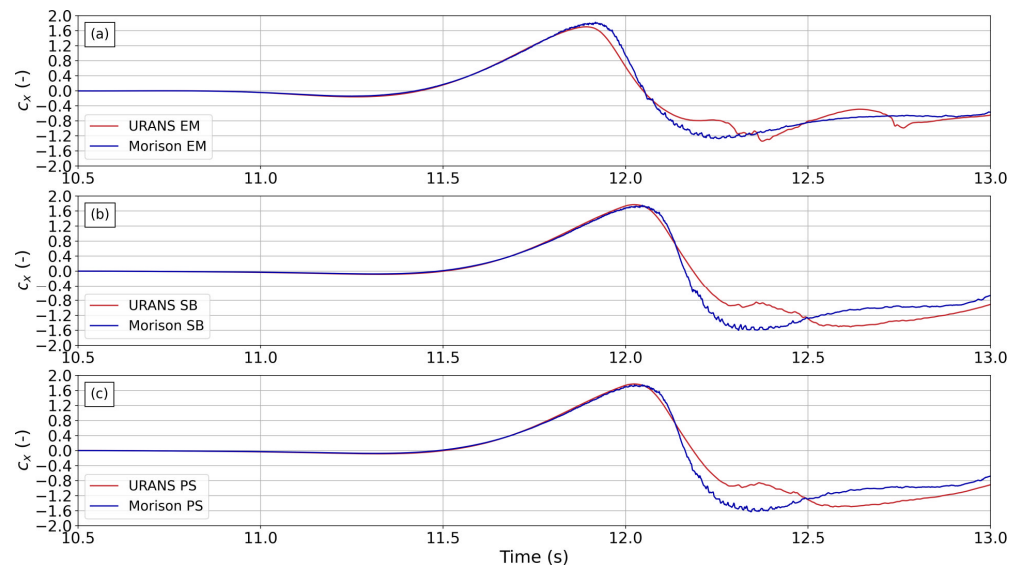


**Figure 16.** Time histories of load coefficient $c_x$ in scenario 2 for the medium-diameter upstream cylinder (**a**), for the medium-diameter downstream starboard cylinder (**b**), and for the medium-diameter downstream portside cylinder (**c**).
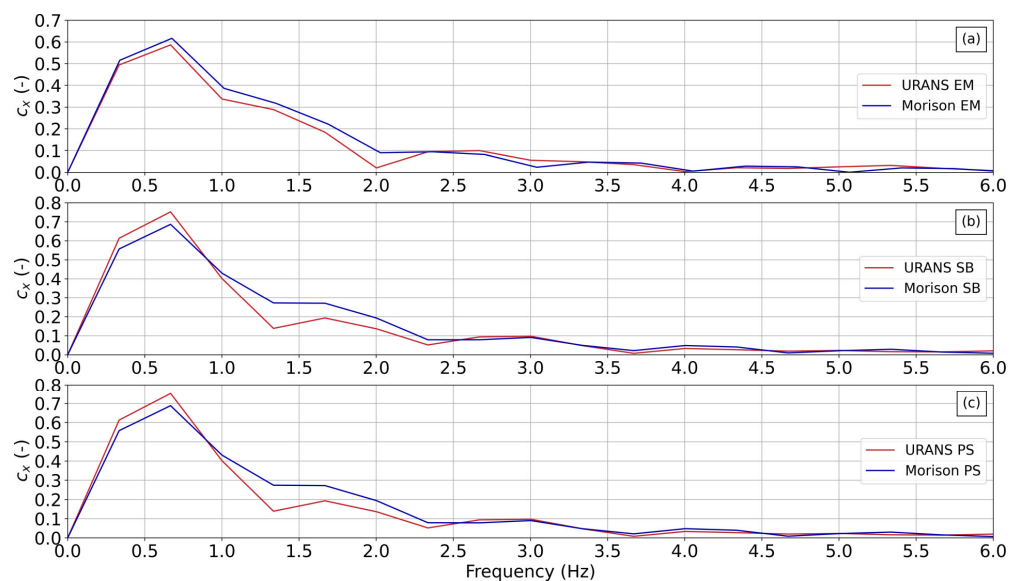


**Figure 17.** Frequency spectra of load coefficient $c_x$ in scenario 2 for the medium-diameter upstream cylinder (**a**), for the medium-diameter downstream starboard cylinder (**b**), and for the medium-diameter downstream portside cylinder (**c**).
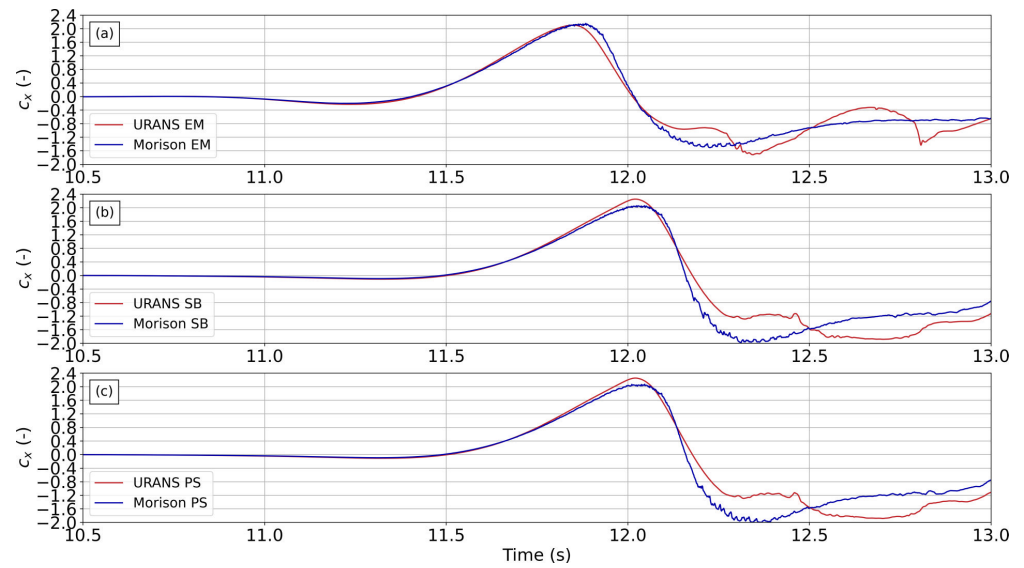
**Figure 18.** Time histories of load coefficient $c_x$ in scenario 2 for the large-diameter upstream cylinder (**a**), for the large-diameter downstream starboard cylinder (**b**), and for the large-diameter downstream portside cylinder (**c**).
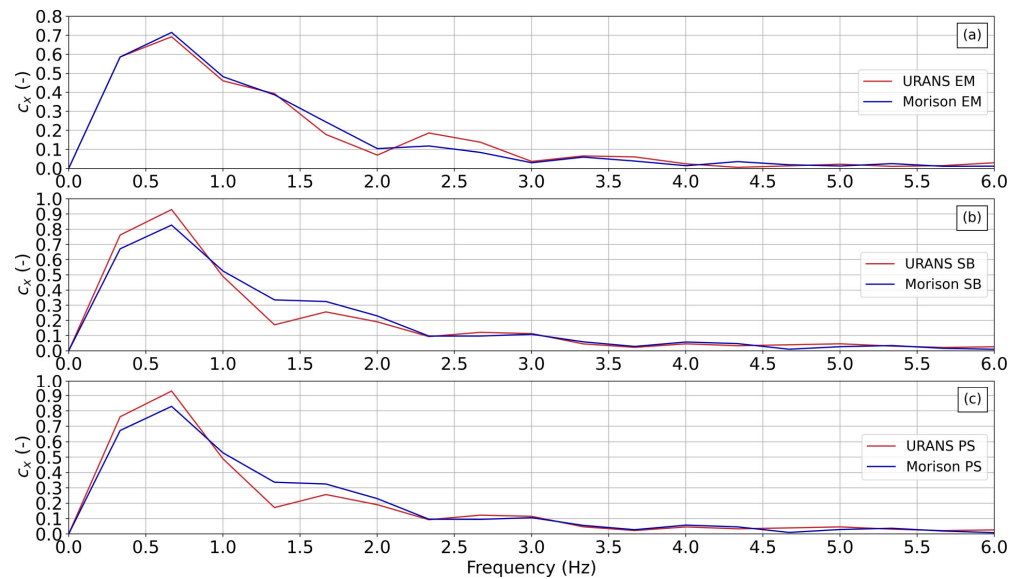


**Figure 19.** Frequency spectra of load coefficient $c_x$ in scenario 2 for the large-diameter upstream cylinder (**a**), for the large-diameter downstream starboard cylinder (**b**), and for the large-diameter downstream portside cylinder (**c**).

Figure 17 presents comparative frequency spectra of load coefficient $c_x$, derived via a fast Fourier transform (FFT), for medium-diameter cylinders in their tripod configuration, i.e., in the second scenario. The first peak of the coefficients occurred at nearly the same frequency for all cylinders, and this peak was slightly higher on the upstream cylinder for the calculations with the Morison equation. The opposite was noticeable for the downstream cylinders. For the upstream cylinder, the two methods yielded coefficients that agreed more closely with each other than for the two downstream cylinders. The greater difference for the two downstream cylinders occurred because the wake and the associated flow interaction between the two transverse downstream cylinders could not be considered by the Morison equation.

Figure 18 presents comparative time histories of load coefficients for the large-diameter cylinders in their tripod configuration, i.e., in the second scenario. For the upstream cylinder,

the impact predicted by both methods matched well. However, this was not so with the load coefficients for the medium-diameter upstream cylinder, see Figure 16. The Morison calculated load coefficients for the downstream cylinders were lower than the URANS coefficients. The temporal progression of coefficients from these two methods matched more closely for the upstream cylinder, which was also so with the load coefficients for the medium-diameter upstream cylinder.

Figure 19 presents comparative frequency spectra of load coefficient $c_x$, derived via a fast Fourier transform (FFT), for the large-diameter cylinders in their tripod configuration, i.e., in the second scenario. For the upstream cylinder, the first peak from the two methods matched favorably. For the downstream cylinders, coefficients from the URANS computations exceeded those from the Morrison equation. This same tendency was also found for the medium-diameter cylinders; see Figure 17. This trend was expected as the missing upstream cylinder in the calculations with the Morison equation was unable to generate a wake on the downstream cylinders. Again, the flow interaction between the two downstream cylinders could not be captured by the Morison equation, because they were not accounted for in these simulations.

Sarpkaya [3,30] investigated drag and inertia coefficients for single cylinders without wake effects and flow interactions between cylinders being installed in a transverse row. Hildebrandt et al. [13] demonstrated that a wake field and flow interaction between cylinders in tandem and in a transverse row affected drag and inertia coefficients. In a previous investigation of ours [11], this led us to consider using the Morison equation for two cylinders in tandem, where an upstream cylinder created a wake field at the location of the downstream cylinder. As only the upstream cylinder was implemented, the downstream cylinder was considered missing. Then the velocities at the downstream cylinder, caused by the upstream cylinder's wake field, were used to calculate the loads acting on the downstream cylinder via the Morison equation. It turned out that this method provided favorable results to efficiently assess impact loads on differently sized downstream cylinders.

Figure 20 presents URANS predicted velocities of the flow field surrounding the implemented tripod configuration made up of the medium-diameter cylinders, taken after a simulation time of 12.0002 s. Streamlines represent these flow velocities located on 37 vertical planes. As seen, flow velocities at the sides of all three cylinders were higher than free flow velocities, and they were accelerated in the gap between the downstream cylinders. The contraction of the streamlines in the gap between the downstream cylinders indicates an acceleration of the flow at this location. This was expected because the fluid flow had to pass through a reduced cross-section.
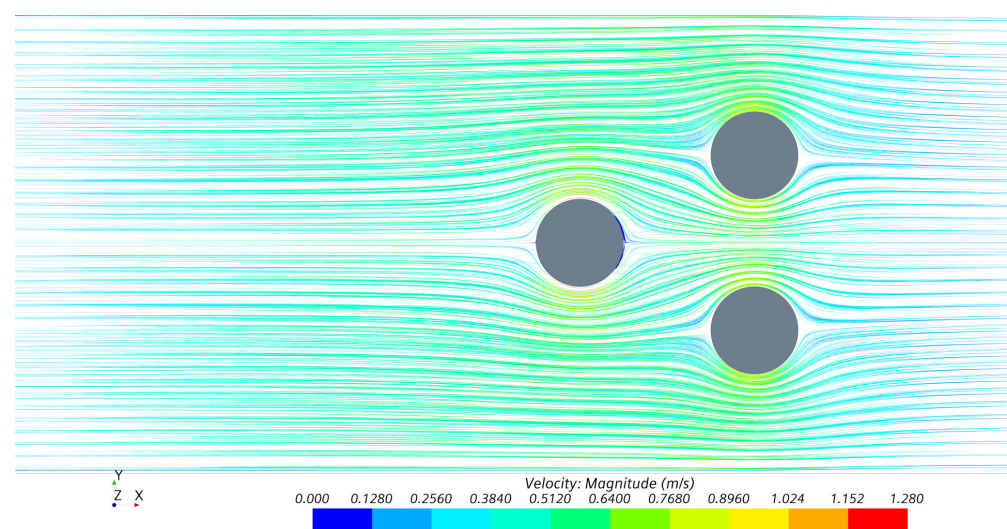


**Figure 20.** URANS predicted flow velocities at $z = -0.074$ m of the flow field surrounding the tripod configuration, consisting of the medium-diameter cylinders, taken after a simulation time of 12.0002 s.

These URANS simulations nicely captured the wake generated behind the upstream cylinder as it influenced the flow past the downstream cylinders. For comparison, Figure 21 presents the simulated streamlines without the presence of the cylinders, taken at the same time. As seen, the flow field was undisturbed as no cylinders were implemented. Of course, the method via the Morison equation could not account for such a phenomenon. The accelerated flow velocities in the gap between the downstream cylinders caused a certain amount of suction, and the influence of this suction was largely responsible for the deviation between hydrodynamic loads acting on the downstream cylinders obtained from URANS simulations and from calculations using the Morison equation.
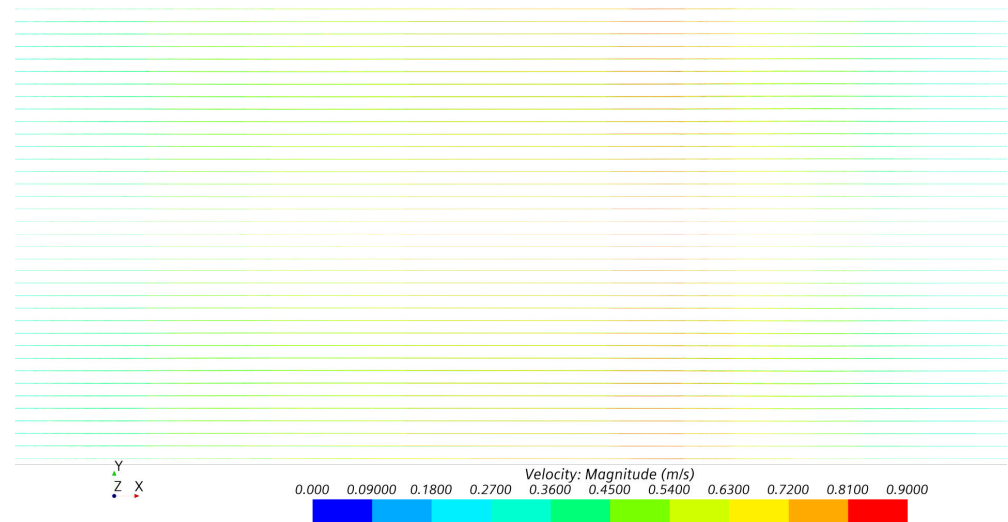


**Figure 21.** Flow velocities at $z = -0.074$ m of the flow field without the tripod configuration, taken after a simulation time of 12.0002 s.

## 8. Conclusions and Outlook

An unsteady URANS solver and the Morison equation were used to predict hydrodynamic loads from a single focused regular wave acting on slender vertical cylinders. The first scenario dealt with single cylinders; the second scenario dealt with three cylinders in a tripod configuration similar to an LNG pump tower.

First, for an individually mounted large-diameter cylinder, preliminary comparative URANS simulations were performed using a laminar and a turbulent flow model. As more accurate results were obtained with the turbulent flow model, this model was chosen for all subsequent URANS simulations.

Experimentally measured loads on two single cylinders of different diameters and different immersion depths were compared to loads obtained from the URANS solver and from the Morison equation. The first load peak was captured more accurately on the large-sized cylinder than on the small-sized cylinder. After the load peak, the URANS-based temporal progression of the load acting on only the large-diameter cylinder compared favorably to experimental measurements. The reduced stiffness of the small-diameter cylinder affected load progression after the load peak.

For the tripod configuration, peak loads on the upstream cylinder obtained from the URANS solver were slightly less than peak loads from the Morison equation. The opposite was the case for peak loads on the downstream cylinders.

Of course, only the URANS simulations were able to capture the wake generated behind the upstream cylinder and the flow interaction between the two downstream cylinders of the tripod configuration. Nevertheless, using the Morison equation yielded loads within an acceptable range of accuracy. However, this accuracy depended solely on the choice of appropriate drag and inertia coefficients.

We demonstrated that a dedicated investigation had to be performed to assess hydrodynamic loads acting on single cylinders in a tripod configuration. This paper dealt with

wake effects on wave induced loads acting on cylinders of different configurations. Such loads may be useful to assess the structural integrity of LNG pump towers installed in partially filled tanks.

**Author Contributions:** Conceptualization, M.T.; methodology, M.T.; software, M.T.; validation, M.T.; formal analysis, M.T.; investigation, M.T.; data curation, M.T.; writing—original draft preparation, M.T.; writing—review and editing, M.T., O.e.M. and T.E.S.; visualization, M.T.; supervision, O.e.M. and T.E.S. All authors have read and agreed to the published version of the manuscript.

**Institutional Review Board Statement:** Not applicable.

**Informed Consent Statement:** Not applicable.

**Data Availability Statement:** From the corresponding author as pre request.

**Conflicts of Interest:** The authors declare no conflict of interest.

## References

1. Morison, J.R.; O'Brien, M.P.; Johnson, J.W.; Schaaf, S.A. The forces exerted by surface waves on piles. *Pet. Trans. AIME* **1950**, *2*, 149–154. [CrossRef]
2. Keulegan, G.H.; Carpenter, L.H. Forces on Cylinders and Plates in an Oscillating Fluid. *J. Res. Natl. Bur. Stand.* **1958**, *60*, 423–440. [CrossRef]
3. Sarpkaya, T. *Vortex Shedding and Resistance in Harmonic Flow about Smooth and Rough Circular Cylinders at High Reynolds Numbers*; Technical Report NPS-59SL76021; Naval Postgraduate School: Monterey, CA, USA, 1976.
4. Champagnac, M.; Gervaise, E. Pump Tower–GTT Methodology for Load Determination for Strength Assessment. In Proceedings of the 24th International Ocean and Polar Engineering Conference, Busan, Korea, 15–20 June 2014; ISOPE-I-14-318.
5. Mehl, B.; Püttmann, A.; Schreier, S. Sensitivity Study on the Influence of the Filling Height on the Liquid Sloshing Behavior in a Rectangular Tank. In Proceedings of the 24th International Ocean and Polar Engineering Conference, Busan, Korea, 15–20 June 2014; ISOPE-I-14-351.
6. Wang, J.; Wan, D.; Chen, G.; Huang, W. Comparative studies of 3-D LNG tank sloshing based on the VOF and IMPS methods. In Proceedings of the 26th International Ocean and Polar Engineering Conference, Rhodes, Greece, 26 June–1 July 2016; ISOPE-I-16-035.
7. Thome, M.; Neugebauer, J.; el Moctar, O.; Schellin, T.E. Assessment of Methods for Calculating Liquefied Natural Gas Pump Tower Loads. *J. Offshore Mech. Arct. Eng.* **2021**, *143*, 61402. [CrossRef]
8. Braeunig, J.-P.; Brosset, L.; Dias, F.; Ghidaglia, J.-M. On the effect of phase transition on impact pressures due to sloshing. In Proceedings of the 20th International Offshore and Polar Engineering Conference, Beijing, China, 20–25 June 2010. ISOPE-I-10-182.
9. Reiso, M. The Tower Shadow Effect in Downwind Wind Turbines. Ph.D. Thesis, Norwegian University of Science and Technology, Trondheim, Norway, 2013. Available online: http://hdl.handle.net/11250/232389 (accessed on 29 August 2022).
10. Blevins, R.D. Forces on and Stability of a Cylinder in a Wake. *J. Offshore Mech. Arct. Eng.* **2005**, *127*, 39–45. [CrossRef]
11. Thome, M.; el Moctar, O.; Schellin, T.E. Wave-induced loads acting on cylinder configurations considering wake effects. In Proceedings of the 41st International Conference on Ocean, Offshore and Arctic Engineering, Hamburg, Germany, 5–10 June 2022; OMAE2022-78835.
12. Sparboom, U.; Hildebrandt, A.; Oumeraci, H. Group interaction effects of slender cylinders under wave attack. In Proceedings of the 30th International Conference on Coastal Engineering (ICCE), San Diego, CA, USA, 3–8 September 2006; pp. 4430–4442.
13. Hildebrandt, A.; Sparboom, U.; Oumeraci, H. Wave forces on groups of slender cylinders in comparison to an isolated cylinder due to non-breaking waves. In Proceedings of the 31st International Conference, Hamburg, Germany, 31 August–5 September 2008; pp. 3770–3781.
14. Li, D.; Yang, Q.; Ma, X.; Dai, G. Free Surface Characteristics of Flow around Two Side-by-Side Circular Cylinders. *J. Mar. Sci. Eng.* **2018**, *6*, 75. [CrossRef]
15. Tong, F.; Cheng, L.; Zhao, M. Numerical simulations of steady flow past two cylinders in staggered arrangements. *J. Fluid Mech.* **2015**, *765*, 114–149. [CrossRef]
16. Sarpkaya, T. Waves and Wave-Structure Interactions. In *Wave Forces on Offshore Structures*; Cambridge University Press: New York, NY, USA, 2010; pp. 109–171.

17. Zdravkovich, M.M. Review of Flow Interference Between Two Circular Cylinders in Various Arrangements. *J. Fluids Eng.* **1977**, *99*, 618–633. [CrossRef]

18. Kimmoun, O.; Brosset, L. Assessment of Morison Equation for Non-Impacting Wave Loads on a Vertical Cylinder. In Proceedings of the 30th International Ocean and Polar Engineering Conference, Virtual, 11–16 October 2020; ISOPE-I-20-3239.

19. Ferziger, J.H.; Peric, M. *Computational Methods for Fluid Dynamics*; Springer: Berlin, Germany, 2002.

20. Ishii, M.; Hibiki, T. *Thermo-Fluid Dynamics of Two-Phase Flow*; Springer: New York, NY, USA, 2011.

21. Menter, F.R. Zonal Two Equations k-$\omega$ Turbulence Models for Aerodynamic Flows. In Proceedings of the AIAA 24th Fluid Dynamics Conference, Orlando, FL, USA, 6–9 July 1993; AIAA 93-2906.

22. Muzaferija, S.; Peric, M.; Sames, P.; Schellin, T. A two-fluid Navier-Stokes solver to simulate water entry. In *Proceedings of the 22nd Symposium on Naval Hydrodynamics*; The National Academies Press: Washington, DC, USA, 1999; pp. 638–651.

23. Leonard, B. The ultimate conservative difference scheme applied to unsteady one-dimensional advection. *Comput. Methods Appl. Mech. Eng.* **1991**, *88*, 17–74. [CrossRef]

24. Bingham, H.B.; Madsen, P.A.; Fuhrman, D.R. Velocity potential formulations of highly accurate Boussinesq-type models. *Coast. Eng.* **2009**, *56*, 467–478. [CrossRef]

25. Madsen, P.A.; Bingham, H.B.; Liu, H. A new Boussinesq method for fully nonlinear waves from shallow to deep water. *J. Fluid Mech.* **2002**, *462*, 1–30. [CrossRef]

26. Madsen, P.A.; Agnon, Y. Accuracy and convergence of velocity formulations for water waves in the framework of Boussinesq theory. *J. Fluid Mech.* **2003**, *477*, 285–319. [CrossRef]

27. Madsen, P.A.; Bingham, H.B.; Schäffer, H.A. Boussinesq-type formulations for fully nonlinear and extremely dispersive water waves: Derivation and analysis. *Proc. R. Soc. A Math. Phys. Eng. Sci.* **2003**, *459*, 1075–1104. [CrossRef]

28. Pestman, W.R. *Mathematical Statistics*; De Gruyter Textbook: Berlin, Germany, 2009.

29. Oberhagemann, J. On Prediction of Wave-Induced Loads and Vibration of Ship Structures with Finite Volume Fluid Dynamic Methods. Ph.D. Thesis, Universität Duisburg-Essen, Duisburg, Germany, 2017. Available online: https://nbn-resolving.org/urn:nbn:de:hbz:464-20170201-090816-5 (accessed on 29 August 2022).

30. Sarpkaya, T. *In-Line Transverse Forces on Smooth and Rough Cylinder in Oscillatory Flow at High Reynolds Numbers*; Technical Report NPS-69-86-003; Naval Postgraduate School: Monterey, CA, USA, 1986.